UiT
THE ARCTIC
UNIVERSITY
OF NORWAY

Department of Physics and Technology

Laser diagnostics of the mesospheric magnetic field

Understanding remote laser magnetometry in northern Norway

—

Alessandra Serrano
FYS-3900 Master thesis in physics, May 2017

For Dr. Raymond Nanni
Thanks for teaching me to mind my units.

ABSTRACT

This thesis outlines initial motivations and propositions for the Mesospheric Optical Magnetometry (MOM) project, using lidar equipment at ALOMAR observatory in northern Norway to initiate a novel technique for measuring Earth's magnetic field at approximately 90 km altitude. Included is an in-depth discussion of the physical phenomena within Earth's mesospheric sodium layer, relevant atomic physics, and laser techniques familiar within the Laser Guide Star (LGS) community. There will be a discussion of the maximization of resonant backscatter from illuminated sodium atoms, including light polarization and optical pumping of sodium. This knowledge is then used to outline the specifications both for the current laser system located at ALOMAR and a new laser system used at Kuiper Telescope in Arizona. Finally, the LGSBloch package for Mathematica will be detailed as a tool for modeling sodium-laser interactions, and simulations of backscatter profiles for conditions at ALOMAR will be presented and discussed.

> *If we teach only the findings and products of science - no matter how useful and even inspiring they may be - without communicating its critical method, how can the average person possibly distinguish science from pseudoscience? Both then are presented as unsupported assertion.... It is enormously easier to present in an appealing way the wisdom distilled from centuries of patient and collective interrogation of Nature than to detail the messy distillation apparatus. The method of science, as stodgy and grumpy as it may seem, is far more important than the findings of science.*
>
> — Carl Sagan

ACKNOWLEDGEMENTS

So much of science goes on behind the scenes, as well as behind the cover of a thesis.

For the myriad people around the world who offered their help in understanding this novel project, I give hearty thanks: James Higbie, for pointing me in helpful directions; Ron Holzlöhner, for his help using the LGSBloch package (and for withstanding my prodding); Tom Kane, Craig Denman and Paul Hillman for discussions about laser hardware and signal-to-noise, and especially Bifford Williams for detailed information on the experimental system at ALOMAR.

Special thanks to those at UiT who helped with this work; Laura Likanen for answering every possible administrative question, and of course, Magnar and Ulf-Peter for slogging through my epically long freakout emails about quantum physics.

To Teebi, Graham, Geoff, Jackie, Danielle, and Devney, for letting me get excited about physics while politely refraining from telling me how nerdy I sound. To Poppet and Mamasita, for being patient with their crazy child running away to the Arctic.

And finally thanks to my brothers, whose mantra of "NEVER LEAVE NORWAY" I'm beginning to seriously take to heart.

CONTENTS

LIST OF FIGURES

LIST OF TABLES

LIST OF PHYSICAL QUANTITES

ω_L	Angular Larmor frequency $[rad/s]$
f_L	Larmor frequency [Hz]
h	Planck's Constant $[J \cdot s]$
$\hbar$	$h/2\pi$
μ_B	Bohr magneton $[J/T]$
g_J	Orbital Landé G-factor
g_F	Hyperfine Landé G-factor

Sodium Atomic Properties

$3^2S_{1/2}$	Sodium ground state
$3^2P_{1/2}$	First excited state
$3^2P_{3/2}$	Second excited state
D_1	Sodium transition from $3^2S_{1/2} \rightarrow 3^2P_{1/2}$
D_2	Sodium transition from $3^2S_{1/2} \rightarrow 3^2P_{3/2}$
D_{2a}	Upper hyperfine split of D_2 line
D_{2b}	Lower hyperfine split of D_2 line

Quantum Numbers

s	Spin quantum number
n	Principal quantum number
l	Orbital angular momentum quantum number
j	l + s
f	Hyperfine quantum number
$m_{s,j,f}$	Spin, orbital, and hyperfine magnetic quantum number
I	Nuclear spin
J	Electronic angular momentum (orbital + spin)
F	Total angular momentum (I + J)

ABBREVIATIONS & ACRONYMS

ADM	Atomic Density Matrix
ALOMAR	Arctic Lidar Observatory for Middle Atmosphere Research
AO	Adaptive Optics
AOM	Acousto-Optic Modulator
BNC	Berkeley Nucleonics Corporation
CW	Continuous Waveform
DFB	Distributed FeedBack
DL	Diode Laser
FADOF	Faraday Anomalous Dispersion Optical Fiber
FASOR	Frequency Addition Source of coherent Optical Radiation
IAGA	International Association of Geomagnetism and Aeronomy
IGRF	International Geomagnetic Reference Field
IMF	Interplanetary Magnetic Field
LEO	Low-Earth Orbit
LGS	Laser Guide Star
LGSBloch	Laser Guide Star modeling program for Mathematica
MOM	Mesospheric Optical Magnetometry
NI-DAQ	National Instruments Data Aquisition
NOAA	National Oceanic and Atmospheric Association
NSF	National Science Foundation
PMT	PhotoMultiplier Tube
PRF	Pulse Repetition Frequency
PSC	Polar Stratospheric Clouds
RFA	Raman Fiber Amplifier
RMR	Rayleigh-Mie-Raman
SHG	Second-Harmonic Generator
TGO	Tromsø Geophysical Observatory

Part I

INTRODUCTORY INFORMATION

This includes a thorough introduction to the various theoretical concepts that lay the foundation for remote laser magnetometry. An exploration of the inspiration and motivation for the concept, and in-depth breakdown of physics regarding Earth's magnetic field, the sodium layer, and relevant atomic physics.

1

INSPIRATION AND MOTIVATION

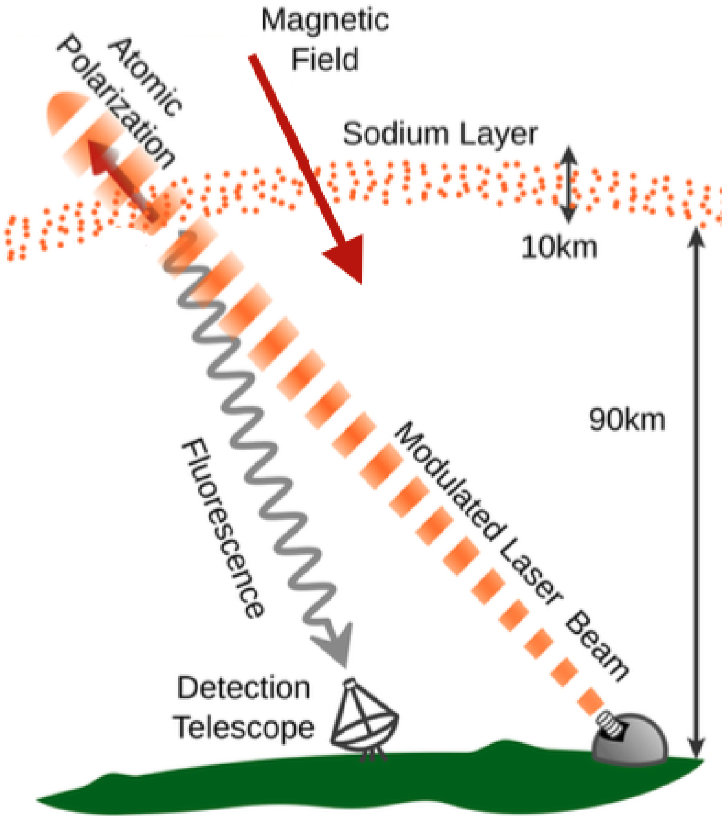

Figure 1: Experimental setup as proposed by James Higbie et al. [30].

1.1 INTRODUCTION

The study of Earth's magnetic field has a long legacy in northern Norway, from early magnetic measurements made in Vardø by Maximilian Hell during the transit of Venus in 1769, to the expedition of *La Recherche* in the late 1830s, to Kristian Birkeland's first scientific observations of the magnetic field and the aurora in the early 20th century[5]. Since Birkeland's time, there have been many developments to methods of monitoring the geomagnetic field, from ground-based magnetometers to Low-Earth Orbiting (LEO) satellites at altitudes between $160 - 2000$ km.

A crucial step toward better understanding Earth's magnetic field is developing a method for making consistent measurements at intermediate altitudes. Such a method was first proposed by Higbie et al. (2010)[29], using the well-developed technical infrastructure of astronomical Laser Guide Stars (LGS) to probe the magnetic field around 90km above Earth's surface. Their proposed experimental setup is pictured in Figure 1, showing a pulsed laser probe and detector measuring backscattered fluorescence from the sodium layer. It is worth going into some more detail on their initial proposal, as it makes a good introduction to this thesis as a whole.

1.2 HIGBIE ET AL.

LGS takes advantage of the naturally-occurring sodium layer in Earth's mesosphere, creating a starlike spot of fluorescence caused by the resonant absorption and backscatter of laser light by the sodium atoms. Higbie et al. connected the physics of LGS with the understanding that mesospheric sodium, acting a magnetic dipole with one valence electron, will also experience a natural precession due to the surrounding magnetic field at a rate proportional to the magnetic field strength. This precession is called Larmor precession, and the frequency of the atoms' precession is called the Larmor frequency.

One can prepare the sodium with laser light resonant with a specific atomic transition, and this in addition causes the sodium to absorb angular momentum and populate an atomic state with their spin-axes oriented in the same direction. This causes the atomic precession to become synchronized.

By thus preparing the sodium and then pulsing the laser beam, Higbie et al. used modeling of sodium atomic processes to show the increase in backscattered light at the point where the laser pulse frequency matches the Larmor frequency. Their model of this phenomenon is shown in Figure 2, with the Frequency axis referring to the rate of laser pulsation, hereafter called *pulse frequency*, *pulse repetition frequency (PRF)*, or *modulation frequency* in order to avoid confusion with other uses of the word *frequency*.[1]

1.2.1 *Further explorations of the method*

The enhancement of LGS technology is an ongoing process. Many of the sources used in this thesis to better understand the resonance signal-to-noise ratio rely heavily on such Laser Guide Star infrastructure.

---

[1] It has come rather painfully to my attention during writing that there is a cornucopia of adjacent terminology that can be extremely confusing. I will endeavor to be as clear as possible in these situations, and have also included explicit clarification in Appendix A.

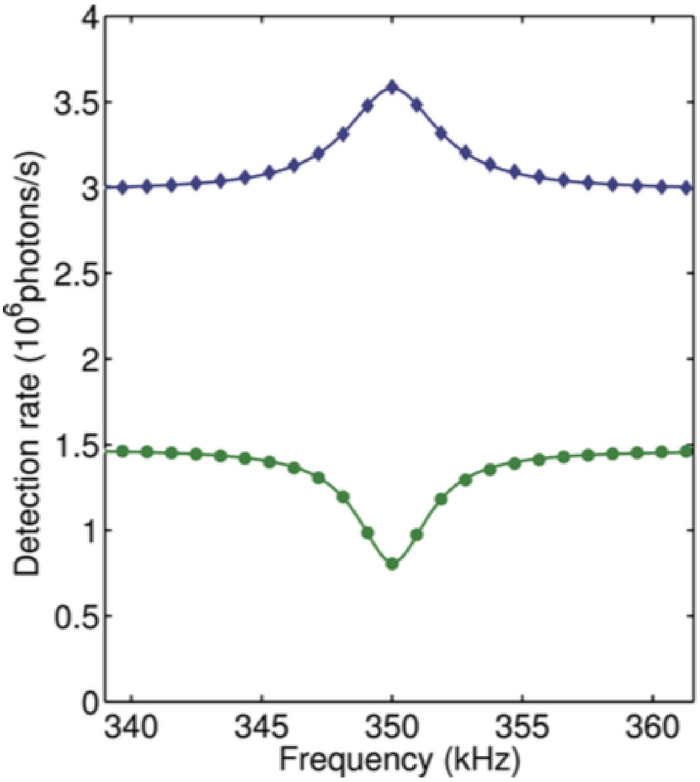

Figure 2: Calculated magneto-optical resonances as shown in Higbie et al. (2011) [30]. The upper curve corresponds to the sodium D_2 transition, while the bottom curve is the sodium D_1 transition. The points are numerical calculations, with a Lorentzian fit overlaid.

Follwing Higbie, Fan et al.(2015)[19] further elaborated on laser backscatter efficiency. Instead of pulsing a circularly-polarized laser beam at the Larmor frequency, Fan et al. showed increased effectiveness of using an electro-optic phase modulator to switch the handedness of circular polarization at a rate of the Larmor frequency. This method is intended to increase LGS return scatter, which could potentially aid in the measure of magnetic field using lasers.

This method proposed by Fan et al. is interesting, but does not reflect our own experimental setup, and is mentioned here simply for completeness.

A main concern for LGS developments is the increase in return scatter. It is also relevant to laser magnetometry in order to optimize signal-to-noise ratio for the resonance peak. This requires some understanding of sodium atomic physics and the interaction with laser light. This is explored in detail by Rachel Rampy in her doctoral thesis[52] and following publications[51, 53]. For simulating the laser-sodium interactions, Rachel Rampy makes use of the LGS modeling program developed by Rochester Scientific[54].

The atomic physics will be more completely discussed in Chapter 3. As we have also utilized the LGS modeling package for laser magnetometry, it will be further explored in Chapter 5 and Chapter 6.

1.3 KANE ET AL.

In the last year, Kane et al.[42] has successfully proven the technique. Using a FASOR[2] laser that was originally built as a LGS prototype, Kane et al. successfully observed the resonance peak, shown in Figure 3, corresponding to the ambient magnetic field strength.

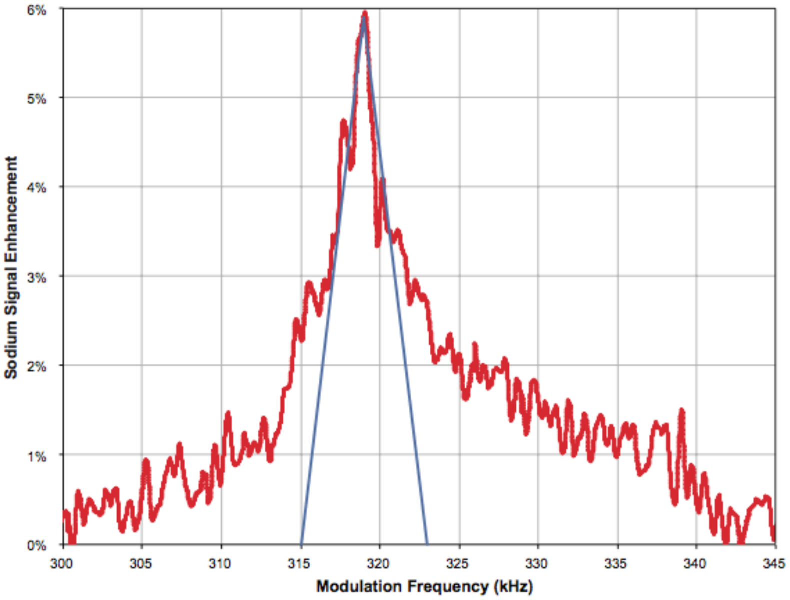

Figure 3: Image of experimental results from Kane et al. (2016)[42]. This figure shows a measurement of the Larmor resonance in the sodium layer, with the blue line as a triangular fit to the data.

Measurements were made using the Kuiper telescope on Mt. Lemmon, outside Tucson, Arizona, USA. Figure 3 shows a resemblance to the proposed Higbie simulations in Figure 2, though Kane et al. prefer to model the resonance peak with a triangle instead of a Lorentzian function. The spread of the peak is much wider than shown in Higbie et al., without showing a strictly "flat" non-resonance region.

In addition to confirming the functionality of Higbie's proposed experiment, this successful measurement helps us to better understand the results of our simulations shown in Chapter 6.

---

[2] Frequency Addition Source of Optical Radiation

1.4 MESOSPHERIC OPTICAL MAGNETOMETRY (MOM)

The ability to measure the magnetic field at this altitude is key to understanding the connection between the magnetic field and the ionosphere. This region is currently only accessible with instrumentation on board rockets, which provide only short-term measurements. There exists no other method for making consistent, long-term measurements at this altitude.

Measurement of magnetic variations in the mesosphere is of particular interest in regions with auroral activity. Remote magnetometry in the auroral zone would provide a tool for monitoring magnetic disturbances in conjunction with the aurora, and for making long-term measurements close to the sources of external field variations, such as Birkeland currents and electrojets [36, 41].

Similar to how Higbie et al. propose to use existing LGS infrastructure for laser magnetometry, the Mesospheric Optical Magnetometry (MOM) project hopes to utilize an existing laser observatory in northern Norway for the same purpose.

Figure 4: Arctic Lidar Observatory for Middle Atmosphere Research (ALOMAR), located in Andenes, Norway. The green laser beams are the RMR lidar. Photo by Trond Abrahamsen, from Andøya Space Center website[11].

Located in the northern island of Andøya, Norway, the Arctic Lidar Observatory for Middle Atmosphere Research (ALOMAR) probes Earth's atmosphere using LIDARs, or laser beams functioning as optical RADAR. There already exists a $10W$ Toptica sodium laser system at ALOMAR, which will be discussed in depth in Chapter 4.

This laser will allow an initial test of the experiment, but will eventually be returned to the owners in the USA. We are fortunate, however, to be in contact with the Kane et al. group, and they have indicated that the laser used in their experiment can be moved to ALOMAR for use in the MOM project.

In the Hardware section of this thesis (Chapter 4), I have therefore outlined a detailed working description of both the current Toptica laser at ALOMAR and that used by Kane et al.

With this introduction to the concept of laser magnetometry and the MOM project, we can now begin a more in-depth discussion of the relevant physics at its foundation.

2

EARTH’S ATMOSPHERE & MAGNETIC FIELD

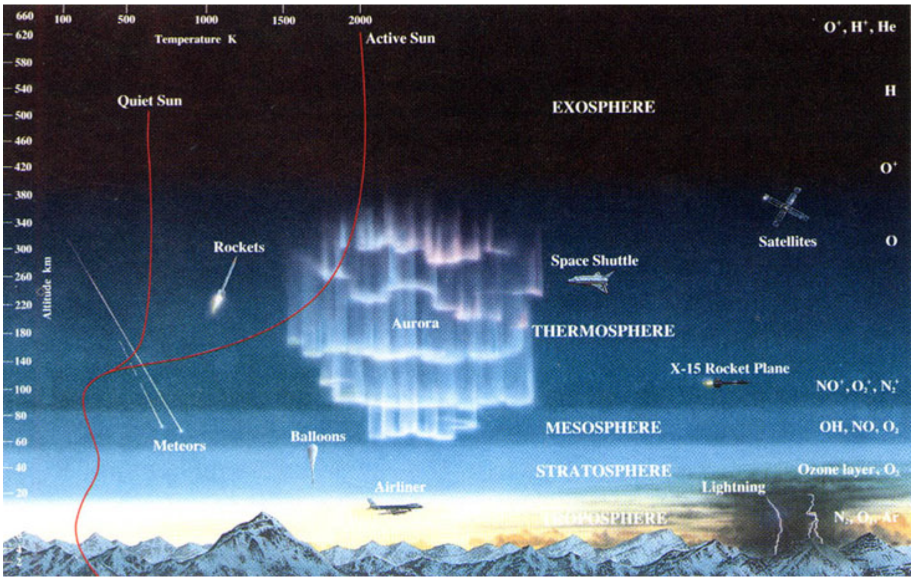

Figure 5: The Layers of Earth’s Atmosphere, including chemistry components and temperature profiles during quiet and active solar activity. Image from HowThingsFly.si.edu[22].

2.1 EARTH’S ATMOSPHERE

The atmosphere surrounding Earth can be considered an ocean of gases enveloping the globe[8].

The atmosphere is separated into different layers, determined by the changes in characteristics such as chemical composition, temperature, or particle density. Figure 5 shows these layers relative to Earth’s surface, standard airplane flying altitude, and height limits for balloons, sounding rockets, and satellites. Critically, the figure also shows the temperature gradients over each layer of the atmosphere.

The layer closest to Earth’s surface is the **troposphere**, where the temperature decreases steadily between 0 and an average 12 km, with variations depending on latitude, season, and weather. It contains more mass than the rest of Earth’s atmosphere combined, and is also denser than any other layer, since as the lowest, it is severely compressed. Its upper boundary is the tropopause, giving way to the stratosphere.

The **stratosphere** extends from the tropopause at 9-17 km to the stratopause at an altitude of about 50 km. As the name suggests, the stratosphere is quite clearly stratified, or layered, with perhaps the most well-known being the ozone layer[17]. Ultraviolet radiation from the sun is absorbed in the ozone layer, causing the upper portion of the stratosphere, and the stratopause, to be significantly warmer than the base, reaching temperatures close to 270 K. Water vapor is much less abundant in the stratosphere than in the troposphere, with only a few parts per million compared to 1000 parts per million, but clouds do exist, called polar stratospheric clouds (PSCs, also called nacreous clouds)[17].

Above the stratopause is the **mesosphere**. Although there is ozone present in the mesosphere, infrared radiation from molecules like CO_2 and CH_4 dominate over the heating from solar radiation. As a result, temperature steadily decreases in the mesosphere region, extending from approximately 50km to 100km[17].

The mesosphere is also the region where most meteors burn up during atmospheric entrance. This phenomenon is responsible for the layer of atomic sodium present in the mesosphere, a layer that has come to play many important roles in modern physics.

Capping the mesosphere is the mesopause, the region where temperature is at a minimum in the atmosphere. The summer polar mesopause is the coldest part of Earth's atmosphere, with temperatures descending even colder than 130 K.

Above the mesopause lies the **thermosphere**, which rapidly increases in temperature with altitude due to radiative ultraviolet energy from the Sun. The thermosphere extends to the thermopause, anywhere between 500-1000 km above Earth's surface, varying substantially based on solar activity.

Surrounding the planet in a thin volume is the **exosphere**, a region where atoms and molecules are still gravitationally bound to Earth, but are of too low density to experience collisions in the manner of a normal gas. This is Earth's uppermost atmospheric layer, with the threshold exobase thinning out until it merges with interplanetary space[62].

The **ionosphere** is a term that includes the upper mesospheric and the thermospheric region, between approximated $75 - 1000$ km. It is defined as the layer of Earth's atmosphere that is ionized by solar and cosmic radiation[12]. The atoms in this area have been ionized by the high solar energy and cosmic rays, leaving positively charged ions and free electrons.

2.1.1 *The Mesosphere & the Sodium Layer*

Compared to lower regions of Earth's atmosphere, the mesosphere remains largely unobserved. The altitude range makes it much more difficult to probe, as balloons cannot ascend above about 35 km. Measurements are restricted to rockets, which provide high-resolution but brief data, satellites, which have limited observation time and low resolution, passive optics such as airglow imagers, and active methods such as radars and lidars[17]. These are used to measure particle densities, temperature, and wind speeds.

The mesospheric region between about 75-110 km contains a multitude of chemical components in addition to oxygen and nitrogen, such as sodium, potassium, iron, magnesium, calcium, and calcium ions (Ca^+). These elements originate from the ablation of meteors.

When meteors and extraterrestrial dust enter Earth's atmosphere, most ablate into metal vapors in the upper mesosphere and lower thermosphere. Because of the high entry velocities of meteoroids, there is high frictional heating due to collisions with air molecules, and their constituents vaporize into the atmosphere. Figure 6 gives profiles of atomic distributions within the mesosphere.

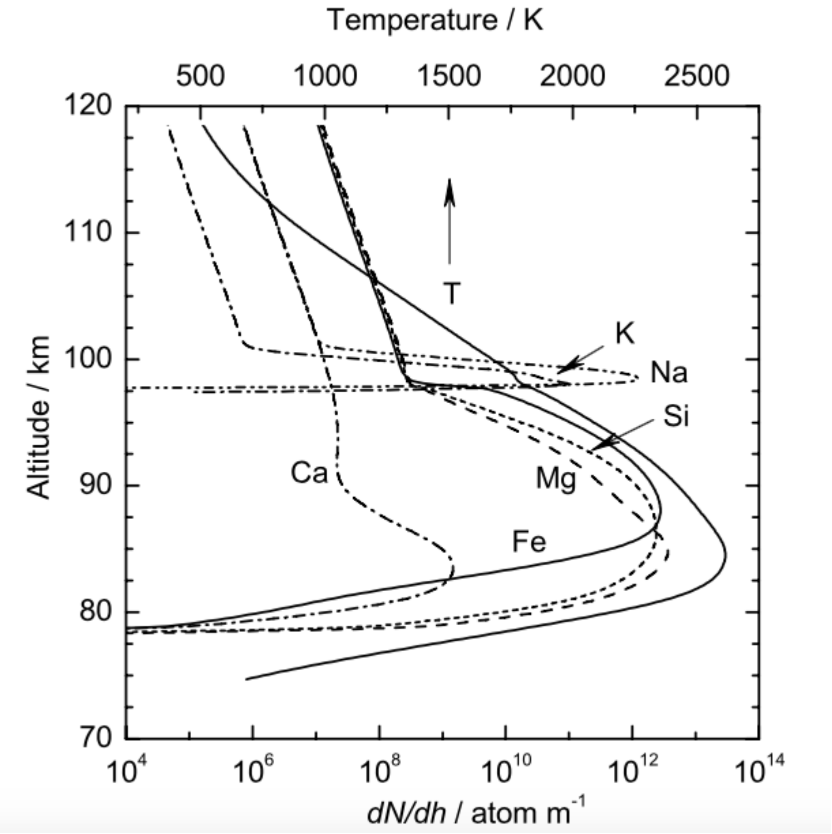

Figure 6: Ablation profiles of different elements from a 5µg meteoroid entering at 20km/s. Figure taken from Vondrak et al.[61].

The figure shows that among these constituents is a thin band of atomic sodium at altitudes of 90-110km, depending on latitude and meteoroid melting temperature. Modeling and lidar data show that the altitude of the Na layer is higher in summer than in winter. An annual mean air density at Andenes at 90 km altitude is approximately $2 \times 10^{-6}\mathrm{kg} \cdot \mathrm{m}^{-3}$, with a typical background sodium number density of about $10^{-22}\mathrm{kg} \cdot \mathrm{m}^{-3}$ in summer, about a fourth of the sodium abundance observed in wintertime[17].

The ALOMAR observatory in Andenes, Norway, has several radars and lidars to effectively measure the mesospheric region. Included is an RMR (Rayleigh-Mie-Raman) lidar used to study winds and temperature in the middle atmosphere, an iron lidar, and the Weber sodium lidar specifically for measurements pertaining to the sodium layer[17]. As will be more thoroughly discussed in Chapter 3, properties of sodium in the mesosphere can be probed by resonantly tuning the laser wavelength to the transitional energy of sodium atoms, at approximately 589 nm[37].

The mesospheric sodium layer has been utilized for many remote sensing applications. The visible emission spectrum makes it ideal for laser measurements, and has been well-utilized for atmospheric lidar measurements, and for removal of atmospheric turbulence at optical observatories (Adaptive Optics).

In order to fully introduce an additional use of the sodium layer, for the purposes of magnetometry, we must now, necessarily, discuss one more component of the mesospheric environment: Earth's magnetic field.

2.2 THE GEOMAGNETIC FIELD

Most of us are familiar with a childhood image of Earth's magnetic field: an apple-shaped ribcage of clear lines that encircle the planet. When discussing the magnetic field, we often neglect how complex a system it truly is. Geomagnetic contributions come from many sources, stretching from Earth's core into space. The majority of surface-level contributions originate internally in the core. Moving upward, there are increasing external sources from the interplanetary magnetic field (IMF), originating from the Sun, as well as magnetospheric currents due to movements of charged particles. The interaction of the IMF with magnetospheric currents is the dynamo that also creates currents in the ionosphere.

The purpose of this section is to summarize the sources most relevant to the geomagnetic field we expect to measure at 90km, and to motivate the desire for further magnetic research in this region.

2.2.1 *Terrestrial Magnetic Field*

The English scientist Edmund Halley (1656-1742) was among the first to compare magnetic measurements and confirm the shift in magnetic north over time[26]. He was able to explain this change by proposing that the Earth itself was composed of two separate magnetic systems,

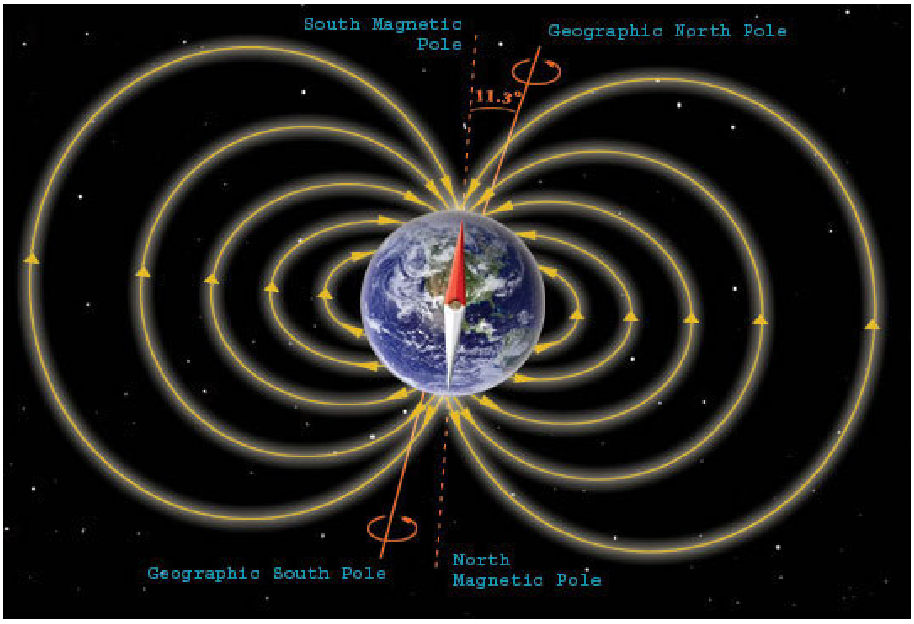

Figure 7: A simplified image showing Earth's magnetic field, the relative angle, and labeling of magnetic poles and geographic poles[56].

one connected to the solid sphere in Earth's interior, and another connected to a concentric spherical shell, or Earth's crust. If these two rotate at different speeds, he proposed, such a drift in the magnetic system could be expected [8].

Near Earth's surface, the magnetic field is indeed approximately a dipole field, as expressed in Figure 7. This magnetic dipole makes an angle of approximately $10°$ to Earth's rotational axis, with geomagnetic poles at $80.0°N, 72.2°W$ and $80.0°S, 107.8°E$ [8].[1]

Since the internal and crustal magnetic fields of Earth are not derivable from a simple analytical function, a model is made from a set of magnetic observations to make a fitting analysis. The customary way is to expand the magnetic potential in a series of spherical harmonics. Magnetic elements are collected from stations across the globe and fitted by the method of least squares, in order to derive coefficients appropriate for Earth's surface.

These coefficients are used, for instance, in the International Geomagnetic Reference Field (IGRF) model of Earth's magnetic field, and is used as a standard reference. The IGRF is used as the source for all our modeling approximations of magnetic field strength and orientation[47].

The geometry conventions of this dipole places the field, rather confusingly, with the magnetic north pole at the south pole, i. e.the magnetic field lines point *out* of the south pole and point *in* to the

---

[1] Note: the geomagnetic poles are distinct from the magnetic poles, which is where a magnetic needle would point vertically.

north pole. This will become relevant when we discuss modeling the geometry of our system, located in the northern hemisphere, in relation to magnetic field lines.

Closer to Earth, this simple dipole model is correct to within about 10% of the real field. This error goes up to within 30% up to a distance of 4 Earth radii [8]. Farther away from Earth, charged particles from solar wind strongly influence the terrestrial magnetic field, shaping it into the magnetosphere.

2.2.2 *Solar-Earth Interactions*

In addition to radiation, the Sun emits a low-density flow of highly conductive particles. This "solar wind" originates in the solar corona, where enormous differentials in gas pressure between interstellar space and the corona force the plasma outward. Figure 8 maps out solar-earth interactions, including the bowshock between solar wind and magnetosphere, and the extended magnetotail facing away from the sun.

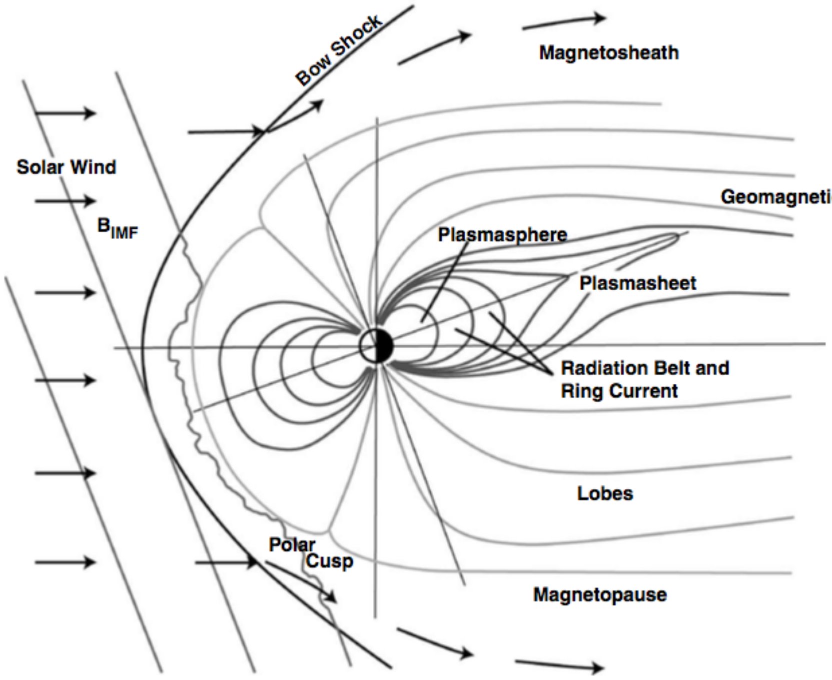

Figure 8: Sun-Earth interaction. Figure from [24].

The Interplanetary Magnetic Field (IMF) is an extension of the Sun's magnetic field that permeates interplanetary space via the charged particles of solar wind. The field is considered "embedded" in the plasma, carried along the field lines originating at the Sun, and dragged outward by the solar wind. As the solar wind varies a lot in velocity and density throughout the solar cycle, so too does the magnetic field.

Velocity can vary between 250 and 800$\mathrm{km/s}$, and the density varies typically between 10^6 and $2 \times 10^7 \mathrm{m}^{-3}$. The magnetic field strength varies between 1nT and 15nT, and is on average 5.5nT[18].

Though the terrestrial magnetic field shields Earth the solar wind, it is also constantly being distorted by it. The high conductivity of solar particles prevents motion across the magnetic field lines, and the solar wind therefore pushes the magnetic field back toward Earth [8]. Figure 8 illustrates the way the dayside magnetic field is compressed, and the nightside field drags into a comet-like tail, appropriately called the magnetotail.

Currents are induced in the solar wind plasma as it moves by the Earth, and these currents give rise to new magnetic fields which add to the terrestrial dipole field. Moreover, the forces exerted by the Earth's magnetic field on the induced currents cause the wind to alter direction so that it avoids the region directly surrounding the Earth [8]. This outer boundary of the magnetosphere, separating the geomagnetic field and terrestrial plasma from the solar wind plasma, is called the magnetopause.

2.2.3 *Ionospheric Currents*

Plasma flow within the magnetosphere is driven by reconnection at the magnetopause between the terrestrial field and the IMF, and consequent related phenomena in the geomagnetic tail[16]. Solar wind and the IMF cause field lines on the day side to become opened, and these lines become pulled across the polar cap by solar winds. They can then encounter the auroral oval region on the night side. Field lines can then reconnect in the magnetopause (day side) and magnetotail (night side), creating plasma flow that can then impose on the ionosphere. Here densities increase enough for collisions to hinder ion movement, allowing electrons to drift and create currents. This plasma flow creates the iconic two-cell current pattern in the ionosphere, seen as twin vortices. This is demonstrated in Figure 9.

Such flow causes collisions between plasma particles and neutral atmospheric particles in the lower ionosphere, causing drag and heating the neutral gas. Because of appreciable plasma densities in the ionosphere, the electrons undergo an $\mathbf{E} \times \mathbf{B}$ drift, resulting in an electric current perpendicular to the magnetic field[16].

Figure 9 also illustrate the Hall currents, flowing around and opposite the path of plasma flow, and the Pederson currents which cross the double-vortex pattern in the direction of the aforementioned electric field.

We can see on the figure points where these Pederson currents converge and diverge, the origin points of upward and downward flowing field-aligned currents.

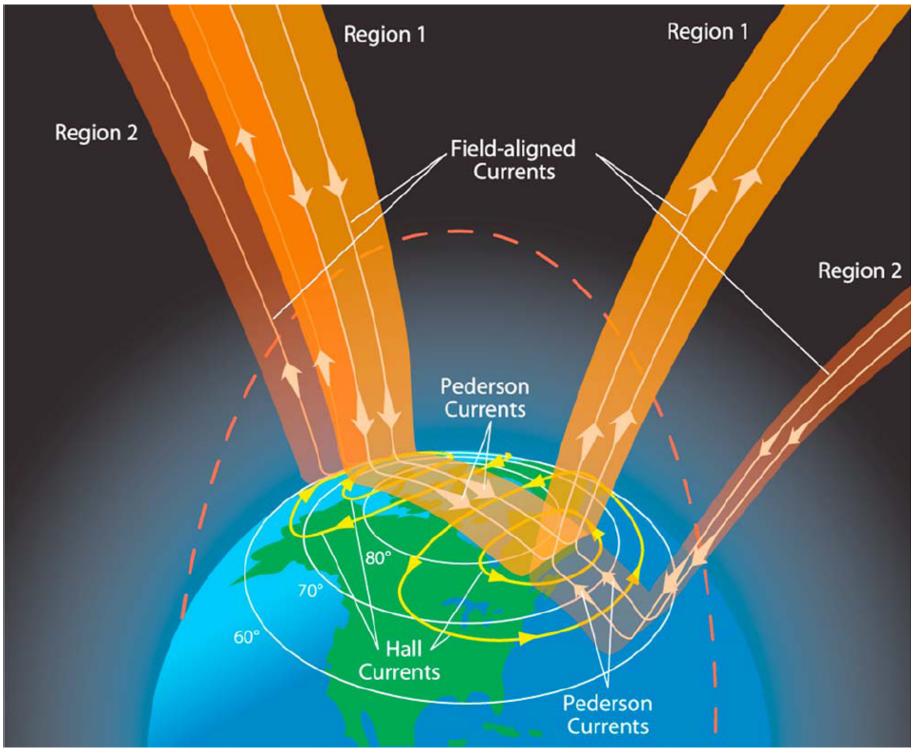

Figure 9: Image from Wikipedia, *Birkeland Current*, showing ionospheric currents at polar regions.

Birkeland currents, or field-aligned currents, have a flow direction associated with the horizontal divergence of Pederson currents. These may flow upward out of the ionosphere, or downward into the ionosphere, along Earth's magnetic field lines. They are responsible for connecting behavior in the magnetosphere to the ionosphere, and were first posited by Kristian Birkeland in 1908[5].

Birkeland, Pedersen, and Hall currents are located in polar regions, and can be roughly represented by Equation 1:

$$\mathbf{J} = \sigma_{||}\mathbf{E}_{||} + \sigma_P\mathbf{E}_{\perp} - \sigma_H\frac{\mathbf{E}_{\perp} \times \mathbf{B}}{B} \tag{1}$$

where $\sigma_{||}$ is the conductivity parallel to magnetic field lines, corresponding to Birkeland currents, σ_P is the Pederson conductivity, σ_H is the Hall conductivity, $\mathbf{E}_{||}$ and $\mathbf{E}_{\perp}$ is the electric field parallel and perpendicular to the magnetic field.

Compared to magnetic field values on the ground, ionospheric currents are very difficult to physically measure, and any existing data has come from satellite observations. It is specifically these high-altitude currents and their connection to the magnetic field that may be better understood through remote laser magnetometry at 90km.

The next section will go into more detail about current methods for measuring Earth's magnetic field.

2.3 MEASURING THE GEOMAGNETIC FIELD

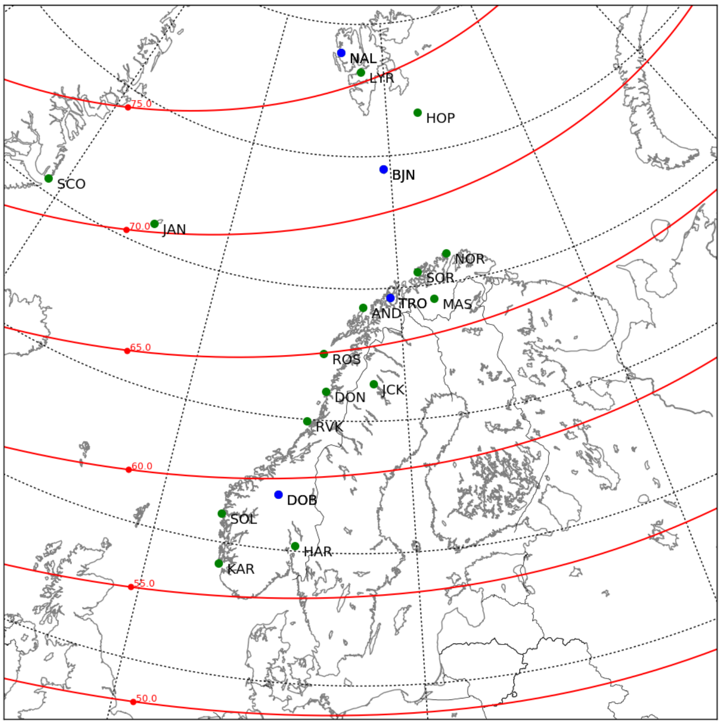

Figure 10: A map of TGO magnetometer locations, with blue dots denoting magnetic observatories, green dots denoting variometer locations, and red lines showing geomagnetic latitudes. Figure from TGO.

Fields on and below Earth's surface have been, and continue to be, studied extensively using ground-based magnetometers across the globe. The Tromsø Geophysical Observatory, for example, maintains a network of ground-based magnetometers stretching across Norway, the Barents Sea, and Svalbard, as shown in Figure 10. Measurements from these magnetometers are extensive and detailed, but are very localized measurements of Earth's surface spread over a large region of sources. Ground-based magnetometers measure the sum of all field sources, i. e., the combination of internal and external magnetic fields at a single point on Earth.

Externally, the magnetic fields have also been measured at Low-Earth Orbit (LEO) altitudes of approximately 160-2000 km, a region that can be investigated by satellites and their instrumentation. Satellite data can provide a large-scale map of these fields, but it is difficult to resolve small currents and fluctuations due to the high speeds ($\approx 9\text{km/s}$) of satellites. Orbit configuration also makes frequent revisiting of the same location difficult.

Between ground-level and 160 km, there is a virtually unexplored region of Earth's magnetic field. This region is unreachable by balloon, and sounding rockets can only achieve short observation time. Magnetic field variations at these intermediate scales give insight to very important scientific phenomena that is especially relevant to polar regions. From here we can learn information about the behavior of Earth's outer mantle and the dynamo in Earth's ionosphere during periods of solar and geomagnetic quiet. It is also possible to use magnetic fluctuations at this altitude to determine large-scale ocean currents relevant to climate and magnetic calibration for navigation [29, 30].

More specifically, magnetometry at these regions can be used to investigate physical processes responsible for carrying energy from solar wind and the magnetosphere to Earth's ionosphere, such as Birkeland currents and relations to the aurora.

2.3.1 *Ground-Based Magnetometers*

Networks of ground-based geomagnetic observatories have existed since Alexander von Humboldt's time in the early 19th century. A good magnetic observatory is a place where precise, continuous, long-term measurements can be made, and provide the backbone of geomagnetic data for the scientific community[43].

The instruments located at ground-based stations measure a sum of both internal and external sources, the core and crustal field with contributions from ionospheric currents and those in the magnetosphere.

There are two kinds of ground stations, namely magnetic observatories and variometer stations. Typically the instruments located at both of these are the same. Variometer stations monitor short-term variations of magnetic fields, while magnetic observatories are very precisely calibrated to monitor Earth's internal magnetic field and resolve the secular variations over hundreds of years. Magnetic observatories therefore also make higher demands on the surroundings, as they need to be in areas free from interference from man-made magnetic material (such as vehicles or metallic buildings).

2.3.2 *Satellites*

The first mission to map Earth's magnetic field at LEO was the NASA MagSat spacecraft, launched in 1979, though it remained in orbit for only about 7 months. Following this are the Danish Ørsted satellite (1999), the German CHAMP (2000) and Argentine SAC-C (2000), all designed specifically for mapping the LEO magnetic field.

Most recently is the Swarm satellite constellation mission, launched in 2013 and operated under the ESA's Earth Explorer Program[50]. This consists of three satellites equipped with magnetometers, flying in formation to form multipoint measurements of Earth's magnetic field, two at a mean altitude of 450 km, and the third at a mean altitude of 530 km.

2.3.3 *A Note On Geometry*

Throughout this thesis, especially when regarding the physical setup of the experiment and our simulations of it, we will have to refer to the geometry of our laser beam probe with respect to the surrounding magnetic field. It is a good idea to have directional conventions in mind, so that at any given point, we know which component of the magnetic field we are considering.

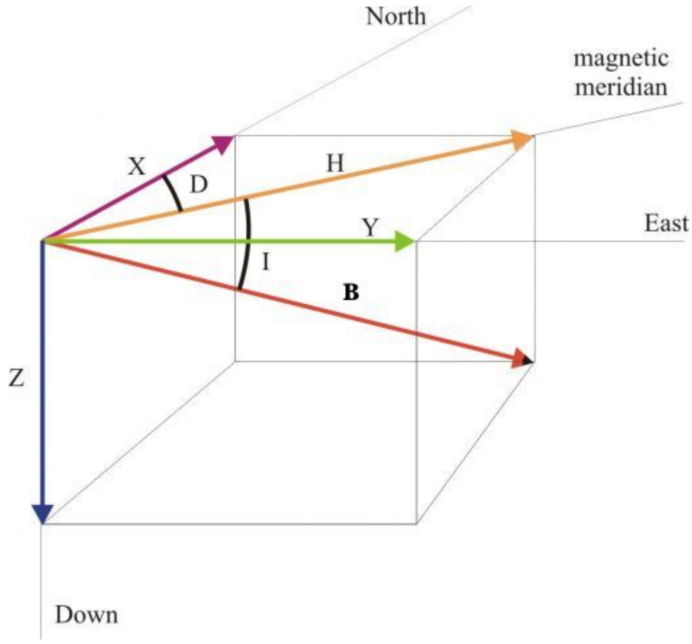

Figure 11: Geomagnetic field components[38].

Figure 11 shows the vector designations for all geomagnetic field components. **B** here corresponds to the total field intensity, **X**, **Y**, and **Z** are the Cartesian coordinates respectively pointing North, East, and at Earth's center. **D** and **I** are magnetic declination and inclination, and **H** represents the total horizontal field component[38]. Primarily within this paper we are concerned with the total field |**B**|, unless otherwise stated.

Measuring Earth's magnetic field at 90km, in proximity to the ionosphere, could for the first time yield detailed information of the temporal variations of Birkeland currents. This is key to understanding the connection between the magnetosphere and the ionosphere.

Equipped with information about Earth's magnetic field and atmospheric environment, we now move on to a discussion of our investigatory instruments – lasers.

3

ATOMS, LIGHT, & LASERS

Figure 12: Laser Guide Star beams cut across the Orion Nebula, as seen from the Paranal Observatory in Chile. Photo by Stéphanie Guisard, through NASA's Astronomy Picture Of the Day.

3.1 ADAPTIVE OPTICS AND INSPIRATION

James Higbie used the already-existing substructure of LGS and AO technology as inspiration for the concept of laser magnetometry. It is only recently that the sodium layer has been utilized for the purposes of observational astronomy. Adaptive Optics (AO) uses high-energy sodium-resonant lasers to excite a spot on the sodium layer as an "artificial star". Astronomers can then use this laser guide star (LGS) to analyze the return backscatter from mesospheric sodium atoms, measure turbulences in Earth's atmosphere, and remove these distortion effects during the imaging process.

The use of laser beams as artificial reference stars was first proposed in 1985 by Foy and Labeyrie[23], and experimentally confirmed by the work of Thompson and Gardner in 1987[59]. Today, the presence of a LGS system is ubiquitous for major observatories.

Figure 12 pictures the four-beam system currently employed at Paranal observatory in northern Chile. We can observe two scattering processes forming the visible laser light in the image. The long "beams" are due to Rayleigh scattering of laser light, while the four separated points are due to resonant absorption with mesospheric sodium and the subsequent emission back toward the direction of laser propagation. It is this second backscatter that is important for both LGS and laser magnetometry, for several reasons.

Ideally, an astronomer wants an LGS that fluoresces at the highest possible altitude, in order to account for the maximum amount of turbulence[53]. It is relatively easy to create a beacon in the atmosphere that is due to Rayleigh backscatter, caused only by the scattering of light off molecules in the air. From our discussion of Earth's atmosphere above, we know that particle density generally decreases with altitude, making a higher beacon more challenging if we depend only on Rayleigh scattering.

This is where the mesospheric sodium layer becomes important. Using a laser with light frequency tuned to 589nm, or the transitional energy of atomic sodium, the sodium can then be excited to produce resonant fluorescence. Sodium is a preferred resonant absorber among the other constituents of the upper atmosphere, since it is both abundant and fluoresces at visible wavelengths[27].

Both LGS production and laser magnetometry depend on optimization of resonance backscatter from sodium, a process which, in order to fully understand, requires a study of the atomic properties of sodium and laser-sodium interactions.

For clarity before going into the specifics of sodium interactions with incident laser light, I will use the next section to outline some general atomic processes and terminology, using sodium as illustration. Following this in each section, we can then discuss the behavior or mesospheric sodium when illuminated by resonant laser light, and finally, its behavior in a magnetic field.

This will lay the groundwork for the final section in this chapter, where we use our understanding of sodium atomic physics to examine laser tactics for optimization of resonant backscatter, including light polarization, optical pumping, and pulsing of the laser beam. I will mirror the order of discussion within the Atomic Physics and Laser Tools sections to elucidate the link from motivations to laser specifications.

3.2 ATOMIC PHYSICS

Naturally occurring sodium in the mesosphere is comprised of virtually 100% one isotope. It contains 11 electrons, of which all but one are in a closed shell[40]. This single valence electron causes the atom to behave as a natural dipole, a structure which will become more relevent in Section 3.2.3. In the following subsections, we will discuss absorption, emission, and angular momentum. Unless otherwise specified (as, for instance, referring to the atomic nucleus), the body in possession of these characteristics is the lone valence electron, though I will sometimes refer to the system as *the atom* to avoid becoming too cumbersome.

3.2.1 *Sodium Atomic Levels*

The most basic and familiar representation of atomic energy levels is shown by the Bohr model, with *fine* splitting of atomic energy levels due to the inclusion of electron spin, and further *hyperfine* splitting caused by the interaction of internal spins and magnetic moments.[1]

These quantized energy levels of a sodium atom are shown in Figure 13, beginning with the Bohr model on the left and progressing to the hyperfine structure on the right. The magnetic quantum numbers m_f are shown across the top, which will be discussed in more detail in Section 3.2.2.

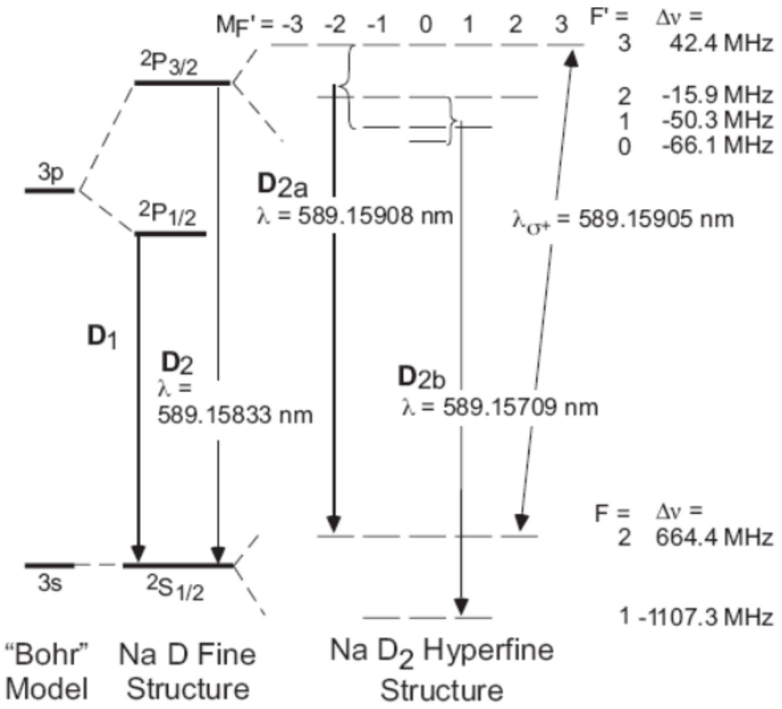

Figure 13: Atomic transitions in the Sodium atom. From Moussaoui et al. [45] and reference therein[32].

Resonance scatter, or fluorescence, is the process of absorption and spontaneous emission of light resonant with the internal energy transitions of the atom. A photon with light frequency equivalent to the energy difference of two atomic levels will excite the atom, and a

---

[1] Not to be confused with effects caused by an *external* magnetic field.

given timescale later, the photon will be emitted spontaneously. For sodium, this excited state lifetime is ≈ 16 ns.

The appropriate light frequency can be calculated using the simple relation

$$E_2 - E_1 = h\nu \tag{2}$$

Where E_1 and E_2 are the starting and ending electron energy levels, respectively.

Sodium LGS takes advantage of the transition between the $3^2S_{1/2}$ ground state and $3^2P_{3/2}$ excited state, known as the sodium D_2 transition[53]. This corresponds to laser light with a wavelength of approximately 589 nm, as shown in Figure 13.[2]

The D_2 line is split into two hyperfine states, the D_{2a} and D_{2b} transition groups. These hyperfine transitions correspond to the F=2 and F=1 ground states, respectively, where the designation F refers to the total angular momentum quantum number of the valence electron.

The D_{2a} transition then has a ground state with a higher angular momentum state than that of the D_{2b} transition. In terms of LGS procedure and our experiment, it will become prudent to have the ability to select which of these hyperfine transitions are excited, and how to account for loss of angular momentum and decay to the F=1 ground state. This will be discussed further in Section 3.3.2.

The following subsection will delve into some quantum mechanics in order to give a physical description of this angular momentum state, and to introduce the idea of how such a state (and therefore, atomic transition) can be selected via polarization of the incident laser light.

3.2.2 *Some Quantum Mechanics*

When discussing the total angular momentum of a sodium atom, we must regard the interactions of various angular momentum components contained within the system: that of the nucleus, the valence electron, and the internal magnetic dipoles formed within the atom. The total angular momentum is then specified along the quantization axis of that particle, in our case, the single valence electron.

In order to become familiar with the vocabulary of atomic angular momentum, let us first define the set of quantum numbers associated the energy states of this electron:

---

[2] When the term *resonant light* is used, it refers to laser light with a wavelength corresponding to this D_2 energy transition. This is an advance notice of the often overlapping terminology such as *frequency* and *resonance*. For extra clarity, I have included an explicit definition-guide in Appendix A.

- **s**, *spin quantum number*. This is the constant, intrinsic angular momentum describing a given particle. For an electron, **s** always equals $1/2$.

- $\mathbf{m_s}$, *electron spin quantum number*. Describes permissible values of **s** along the quantization axis. In the case of an electron, this is either $-1/2$ or $+1/2$. The total electron spin is the quantum number multiplied by $\hbar$, the reduced Planck's constant, a unit of proportionality between the momentum and quantum wavelength.

- **n**, *principal quantum number*. This describes the energy state of a given particle, i.e., the excitation level or "shell". This can be changed by modifying the incident light wavelength to correspond to different energy transitions, as in Equation 2.

- **l**, *orbital angular momentum quantum number*. This describes the shape of the orbital that the electron occupies, and so the angular distribution. It divides **n** into subshells.

- $\mathbf{j} = \mathbf{l} + \mathbf{s}$. This represents the combination of **l** and **s**, and is my preferred notation, both because it includes more information, and also avoids confusion between **l** and the number 1.

- $\mathbf{m_j}$, *magnetic quantum number*. This value ranges in integer value from **-l** to **+l**. This value describes the fraction of the angular momentum **l** along the quantization axis. This is the value that can be modified using laser light polarization, as will be discussed below. (Equivalent to above, I will use $\mathbf{m_j}$ instead of $\mathbf{m_l}$ for the magnetic quantum number.)

- **f**, *hyperfine quantum number*. This describes what are essentially energy levels within the energy levels **j**. With light tuned finely enough, these hyperfine transitions can be distinguished.

- $\mathbf{m_f}$, *magnetic hyperfine quantum number*. This is the hyperfine equivalent of $\mathbf{m_j}$.

To summarize, **s** specifies what kind of particle we are discussing, while **n,j,f** specify the unique quantum state of that particle. These are *quantum numbers*, which in turn correspond to the selected atomic states **I, J, F** by a factor of $\hbar$, illustrated in Figure 14. The total angular momentum of a particle is then given by vector addition of the component angular momenta[9], as visualized in Figure 15.

This will become relevant in Section 3.3.2 when we discuss ways that we can affect the angular momentum via laser light. In this way, we are transferring energy to the sodium atom via photons. The light wavelength alters the energy level **j**, while changing $\mathbf{m_j}$ is more complicated. This can be achieved, however, by polarizing the incident light.

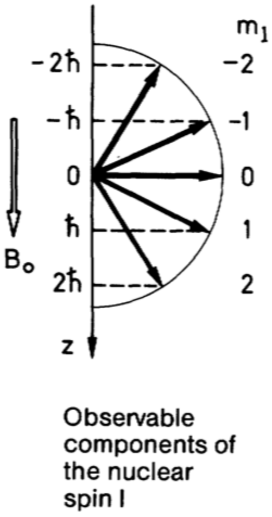

Figure 14: A visualization of vector angular momentum quantum numbers, and how they correspond to physical values of angular momentum. Figure from *The Physics of Atoms and Quanta*[25].

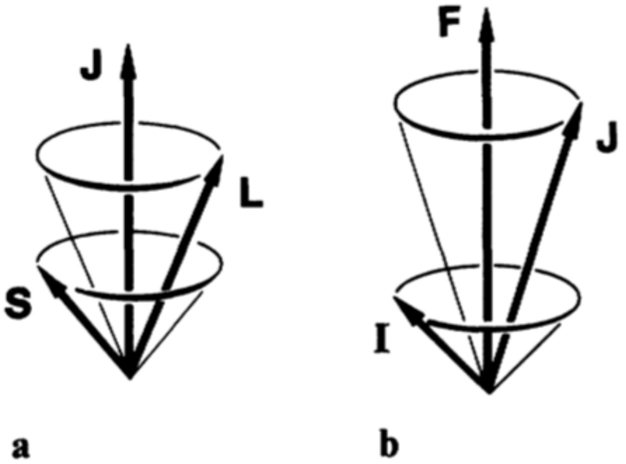

Figure 15: A visual showing coupling of a) the **S** (spin) and **L** (orbital angular momentum) vectors to total electron angular momentum **J**; and b) coupling of **J** (electron angular momentum) and **I** (nuclear angular momentum) to create the total angular momentum **F**. Figure from *The Physics of Atoms and Quanta*[25].

Before our full discussion of laser techniques, I will continue by describing the behavior of sodium atoms in an ambient magnetic field, as is the case in the mesosphere.

3.2.3 *Behavior in an External Magnetic Field*

Within our sodium dipole, there is an internal magnetic moment, created by a combination of the nuclear magnetic moment and the magnetic field which the electrons produce at the site of the nucleus[25]. This magnetic dipole points along the axis of total angular momentum (**F**), as discussed in the previous subsection.

This is not to be confused with an external magnetic field which may be interacting with that dipole. An external field will have two related effects on the sodium atom. First, the external field adds to the internal field, resulting in a splitting of each energy level into the hyperfine states. This is called the Zeeman effect[25]. Effectively, the magnetic dipole moment associated with each angular momentum quantum state is separated by the magnetic field into distinct energy levels[49]. The size of the splitting is dependent on the strength of both the internal magnetic moment and the external magnetic field.

The total angular momentum vector **F** will precess about the magnetic field lines **B**, with the orientation of **F** about **B** given by the magnetic quantum number $\mathbf{m_F}$ as defined in the above section, similar to that shown in Figure 14. This is the Larmor precession.

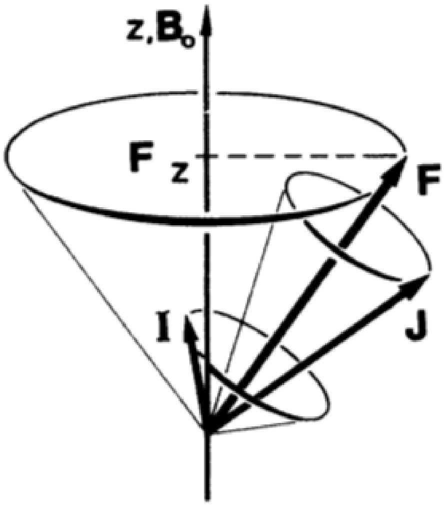

Figure 16: A representation of the vector addition of atomic angular momentum components to form the total angular momentum **F**, which then undergoes Larmor precession when subjected to an external magnetic field **B**. Figure from [25].

All atoms (or particles) with a magnetic moment will experience Larmor precession when subjected to a magnetic field. The magnetic moment will feel a torque τ, equal to $\mathbf{F} \times \mathbf{B}$, which tries to bring it in line with the field direction. But the atomic magnet behaves like a gyroscope – it has the angular momentum **F**. Therefore the torque due to the magnetic field will not cause the magnet to line up, and instead will precess about the axis parallel to the external magnetic field[21]. This behavior is the key mechanism behind laser magnetometry, and measuring the rate of Larmor precession is analogous to measuring the surrounding magnetic field strength.

The Larmor frequency for a given atom can be calculated with a simple equation. We are interested in calculating the value for a sodium atom in its $3^2S_{1/2}$ ground state, as this will be the naturally occurring state when acted upon by incident laser light[45]. Since the Larmor frequency will later translate to the frequency at which our laser will be pulsed, I have opted for the non-angular expression f_L:

$$f_L = \frac{g_F \mu_B B}{h} \tag{3}$$

where μ_B is the Bohr magneton, a constant, B is the external magnetic field, and h is Planck's constant. g_F is the hyperfine Landé factor.

The Landé g-factor is a proportionality constant that describes the magnetic moment and gyromagnetic ratio of a particle, with the hyperfine version (g_F) specifically for an atom with total angular momentum $F = I + J$. I will first state the equation, so it may be more obvious to the reader where this discussion is headed:

$$g_F = g_J \left[\frac{F(F+1) + J(J+1) - I(I+1)}{2F(F+1)} \right] \tag{4}$$

g_J is a factor derived from the initial energy state of the atom, in our case, the ground state of sodium, and so $g_J = 2$. F, J, and I were discussed previously, and their values are well defined for the sodium atom as follows:

J describes the total **electronic** angular momentum, which combines information on the orbital angular momentum and the spin of the valence electron. For the ground state, $J = 1/2$

I is the **nuclear** spin of our sodium atom. Since the naturally occurring sodium in the mesosphere exists virtually 100% as one isotope, we know for all mesospheric sodium that $I = 3/2$.

F, or the **total** angular momentum, describes the interaction between the electron and the nuclear magnetic moment. It is simply the sum of the electronic spin J and the nuclear spin I,

$$F = I + J \tag{5}$$

so in our case of the sodium D_{2a} ground state, $F = 2$.

With this information, we can use Equation 5 to find the value $g_F = 1/2$ for the $3^2S_{1/2}$ ground state. From this, we refer to Equation 3 to find that the Larmor frequency is directly proportional to the surrounding magnetic field by a factor of

$$f_L = (7 \times 10^9)B \tag{6}$$

with B given in units of Tesla, and f_L in Hz. This proportionality factor is the *gyromagnetic ratio*. The Larmor period, or timescale for one rotation at Larmor frequency, can be given by

$$\tau_L = \frac{1}{f_L} \tag{7}$$

where τ_L should not be confused with the torque exerted on the magnetic field, τ.

Measuring the Larmor frequency of mesospheric sodium is at the crux of the process of remote laser magnetometry. The following section will delve into how LGS and laser technology has made use of the atomic physics discussed in this section in order to interact optimally with mesospheric sodium, and how to exploit these atomic properties to measure the magnetic field strength.[3]

3.3 LASER TECHNIQUES

Since the first experiments for LGS in the late 1980s, methods have been developed to increase resonant backscatter by navigating the atomic properties of mesospheric sodium. This section will use the information covered in the previous to present laser techniques, with subsections in the same order as those of the relevant physical processes in the previous section. I. e., Section 3.3.1 will define laser techniques corresponding to atomic properties presented in Section 3.2.1, etc., to simplify any review.

First we will discuss the wavelength of laser light needed to create sodium fluorescence. Second, we will explore how to select the optimal sodium transition for maximum backscatter, by means of laser polarization and optical pumping, or tuning a small percentage of laser light to a second transition. Finally, we will discuss amplitude modulation, or pulsing, of the laser beam, in order to achieve a resonance peak that exposes the atomic Larmor frequency.

3.3.1 *Resonance Fluorescence*

It is quite simple to assert that, in order to excite sodium and cause it to backscatter, we want laser light that is resonant with the energy transition. But as we've seen from study of the atomic structure of

---

[3] I have included lookup tables for the Larmor frequency corresponding to external magnetic fields similar to those found on Earth. This can be found in Appendix B.

sodium, we have to ask the question: which transition do we mean? Referring back to Figure 13 shows us both the D_1 and D_2 transitions, and the hyperfine D_{2a} and D_{2b} lines, all with an individual excitation wavelength.

LGS takes advantage of the $3^2S_{1/2} \rightarrow 3^2P_{3/2}$ transition, or D_2 line. The ground state consists of two hyperfine multiplets, with 8 magnetic substates combined[53]. Fluorescence from this transition can be achieved by tuning the laser wavelength to the D_2 transitional energy, at 589nm.

At mesospheric temperatures, around 200K, motion of the sodium atoms Doppler broadens the two D_{2a} and D_{2b} transition groups emission lines into a two-peaked fluorescence profile, as shown in Figure 17.

A laser beam with linewidth, or distribution of photon wavelength, smaller than the spread of about 1 GHz can resolve these two transitions.

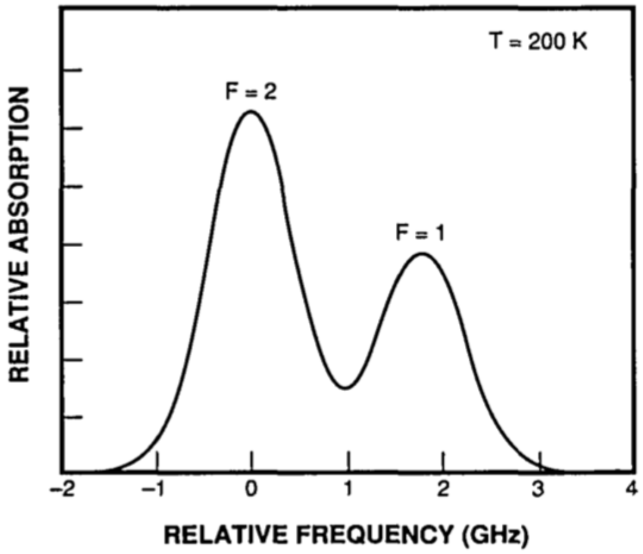

Figure 17: Absorption profile of the D_2 sodium line, Doppler shifted for mesospheric temperatures around 200K, with F=1 and F=2 ground states resolved. Figure from Jeys 1992[39].

Revisiting Figure 13 and the sodium atomic structure, we can see that a sodium atom excited with the D_2 energy can relax back down to either of two ground states. Given a few excitation-relaxation cycles, virtually all the atoms will fall to the **F**=1 ground state, no longer in resonance with the incident radiation, and undergo no further transitions[39]. The sodium layer will, after short timescales, become optically transparent to a laser probe, unless a mechanism can be utilized to raise the mesospheric sodium into the **F**=2 ground state.

This can be achieved via polarization of the incident laser beam, in a process known as optical pumping.

3.3.2 *Light Polarization & Optical Pumping*

The basis of the process of optical pumping is to apply polarized laser light so that the photons will transfer angular momentum to the valence electron. Once this happens, the lowest available energy state is one with more than the minimum allowable energy. Upon optical pumping, the atom is said to be *oriented* in a particular sublevel. We will discuss the specific meaning of *orientation* in this context shortly.

Simon Rochester[55] lists three ways that this atomic orientation is beneficial for photon return:

1. The D_{2a} transition is the strongest, and so the effective absorption cross section is increased.
2. Atoms excited in this cycling transition cannot spontaneously decay to the **F**=1 ground state, where they would no longer interact with light.
3. Fluorescence from this transition is preferentially directed along the light beam, leading to an enhancement of photon flux observed at the location of the light source.

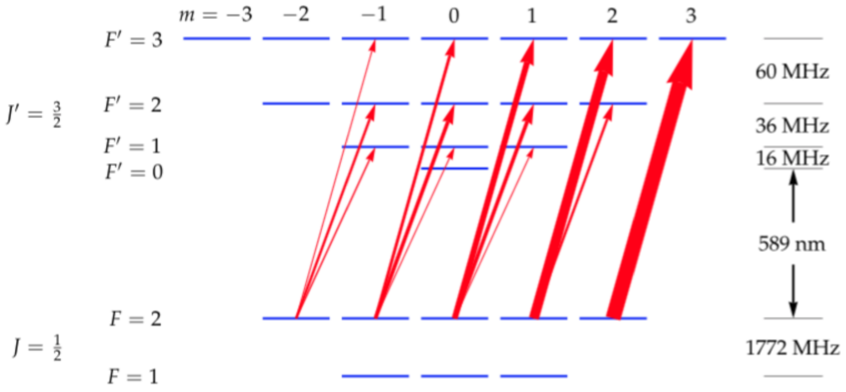

Figure 18: Graphical representation of excitation transition probabilities. Figure 2 from [40]

How does polarization of the incident laser light orient an atom? To understand this process, we must recall the magnetic quantum numbers discussed in Section 3.2.2. During the excitation and relaxation process, atomic selection rules dictate which magnetic quantum states an electron may inhabit, and this is directly influenced by the light polarization. Because of this, emission from certain substates are inherently stronger than others. Figure 18 visualizes these magnetic substates for the hyperfine transitions, with a level diagram showing the relative strength of each transition.

The light polarization "permits" different values of the magnetic quantum number, which in turn increase the probability of certain transitions when the electron decays back down to the ground state. For a thorough mathematical breakdown of this process, see Auzinsh et al.[2], and for tables of all sodium transition probabilities, see Daniel Steck[57]. Other good references are Hawkins(1955)[28] and *Physics of Atoms and Molecules* by Brandsen and Joachain[7].

The concept is, however, summarized very nicely by Moussaoui et al. (2009):

> Each of the [hyperfine] levels splits up into $2F + 1$ magnetic quantum levels. For linearly polarized light, only transitions with $\Delta m = 0$ are permitted, whereas for circularly polarized light, Δm must be either $+1$ or -1. Atoms at a given **m** level in the upper state can fall back according to the rule $\Delta m = -1, 0, +1$. In the presence of a [circularly] polarized laser beam, for instance, populations migrate toward the $F = 2 \leftrightarrow F = 3$ states, and this transition has the largest relative oscillator strength [45].

In order to visualize this, we look again at Figure 18. Linearly polarized photons, with $\Delta m = 0$, can only create transitions along a "straight" line, whereas circularly polarized photons, with $\Delta m = \pm 1$, move along a "diagonal". The direction depends on the handedness of the circularly polarized light. Over a few excitation and decay cycles, sodium electrons excited with circularly polarized light will preferentially populate one of the "wings", while depopulating **m** states in the center.

The goal of orienting the atomic population is to have greater control over the resulting decay transitions. By controlling which levels the sodium electrons decay from, we can then manage the preferred direction of the emitted photons.

However, despite this meticulous presentation, there is still the loss of angular momentum in the mesosphere due to collisions. In this case, 3/8 of the sodium atoms can relax down to the **F**=1 ground state, becoming lost to the excitation process tuned to the higher ground state.

To counteract this process is the act of *repumping*, or tuning a small percentage of the laser light to interact with the D_{2b} transition to reintroduce those atoms into the cycle of excitation and emission[52]. Figure 19 gives a visual representation contrasting the ineffectiveness of linearly polarized light with the process of optical pumping using circularly polarized light, including repumping process.

Optical pumping plus this repumping process allows the majority of atoms to become trapped in this desired two-state cycle, minimizing eventual decay of sodium fluorescence.

This is the definition of *orienting* an atom or atomic population.[4] The total angular momentum of sodium is preferentially oriented to

---

[4] See Appendix A for a more pedantic definition of orientation.

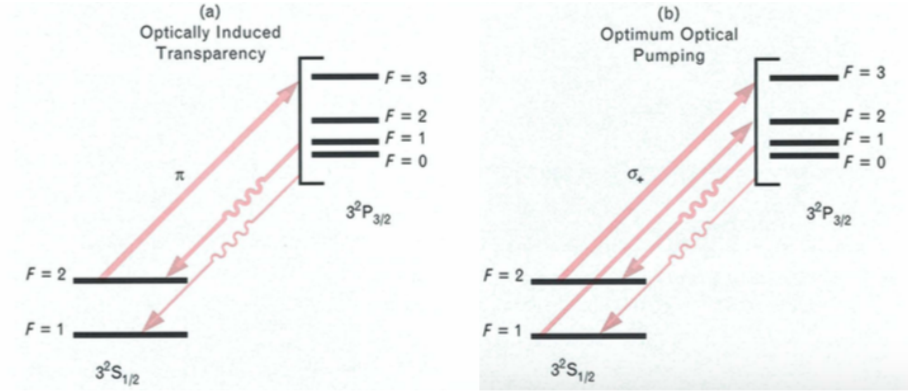

Figure 19: **a)** Inefficient resonance of sodium using linearly polarized light, and **b)** optimal optical pumping with repumping scheme, using circularly polarized light. Figure 5 from [40].

the strongest transition of the entire D2 group, and it is forbidden by selection rules from decaying to the **F**=1 ground state. Further demonstrations of this fact by statistical analysis of sodium transitions can be found in in Steck(2000)[57].

Pumping with circularly polarized light also has the benefit of orienting the sodium vapor in such a way that the fluorescence is directed preferentially along the light beam[52]. This is demonstrated in Figure 20, contrasted with the effects of linearly polarized light.

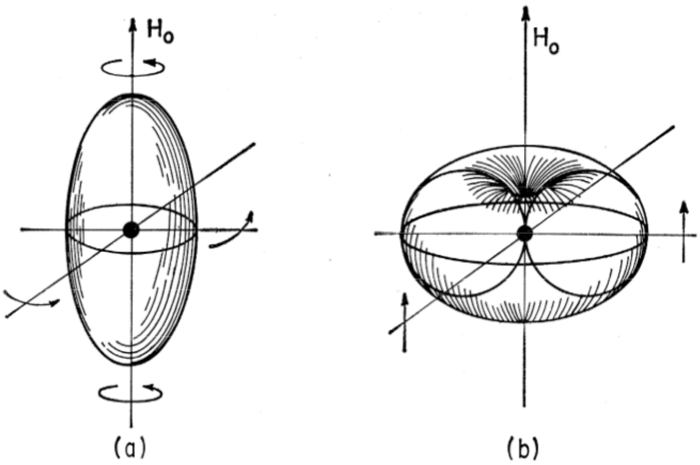

Figure 20: A plot of the angular distribution of the electric vector amplitude in electric dipole radiation for *(a)* circularly polarized light ($\Delta m = 1$ transitions), and *(b)* linearly polarized light ($\Delta m = 0$ transitions), showing the direction of the electric polarization of the emitted light. Figure from Thomas R. Carver[10].

Figure 20 is a visual representation of the atomic angular momentum distribution, with the length of the radius representing the probability of orientation in a given direction[54]. This is equivalent to the directional preference of return fluorescence[52], and we can see those pumped with circularly polarized light (a) return along the laser beam axis, i. e., back toward the viewer.

The benefits of optical pumping and repumping can, however, be diminished by other effects. The natural Larmor precession due to Earth's magnetic field is referred to as an "evil" that can thwart optical pumping[34].

The technique of amplitude-modulating, or pulsing, the laser beam at the Larmor frequency is used to mitigate this loss.

3.3.3 *Pulsing the Laser Beam*

When a magnetic moment is directed at some angle with respect to the magnetic field direction, the field then exerts a torque on the magnetic moment. This will cause it to precess about the magnetic field direction, as shown in Figure 21, similar to the precession of a spinning top around the field lines of gravity.

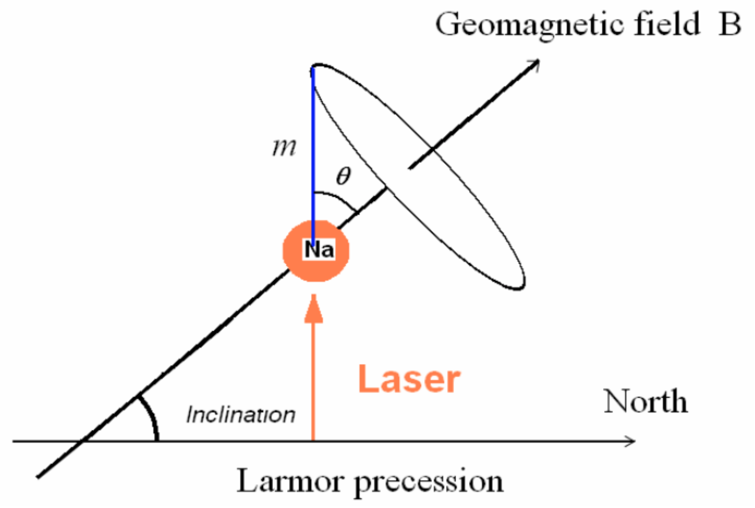

Figure 21: The geometry of atomic Larmor precession about the magnetic field lines. Figure from Moussaoui et al.[45]

This precession also causes the system to lose energy, and atoms to eventually become lost by relaxing to the **F**=1 ground state[34].

Pulsing a laser beam at the Larmor frequency is used to combat the destruction of the repumping process. Pulsing the beam enhances the repumping process – or, more specifically, it presents the atoms in a state where the destruction of repumping has not taken effect. This is best explained in the pioneering paper on optical pumping by Bell & Bloom:

> One can picture the effect as follows. If one takes a "snapshot" of the system at *t*=*0* in a time short compared with a

> Larmor cycle, the effect of H_0[the magnetic field] is a negligible perturbation and the light "pumps" a small amount of polarization in the *x* direction. This polarization immediately starts to precess in the *xy* plane at the Larmor frequency and is added vectorially to the polarization produced at all other instants of time. For unmodulated light this vector sum is clearly very small or zero. If the light is modulated at the Larmor frequency, however, then the polarization produced at *t=0* is not exactly cancelled by that produced at $t = \pi/\omega$ and is reinforced by the polarization produced at $t = 2\pi/\omega$, $4\pi/\omega$, etc. An equivalent point of view is to consider the system in a coordinate system rotating at ω; since the "rotating" lamp is turned on only when it is pointing in a certain preferred direction, it is effectively stationary in a frame of reference for which the effective magnetic field is very weak. Optical pumping then takes place as if the effective field were parallel to the light beam[3].

Pulsing the incident laser light at the Larmor frequency compensates for the loss of optical pumping by re-synchronizing the atomic angular momentum at the rate they are naturally precessing.

With this in mind, we can return to the subject of laser magnetometry, and the iconic resonance peaks simulated by Higbie et al. and measured by Kane et al. When the laser is pulsed at a frequency that matches the Larmor frequency, we experience a peak in sodium fluorescence because of how it mitigates the depletion of optical pumping benefits.

3.4 LASER GEOMETRY

We now have information about the atomic processes of mesospheric sodium and how our laser beam can most effectively interact with these processes. Before moving on to talk about our laser systems, there is one last consideration: the unique high-latitude position of ALOMAR observatory, and the geometry of our laser beam with the magnetic-field aligned atomic precession.

The majority of observatories that utilize LGS are located at relatively low latitudes, with the magnetic field lines close to horizontal at the mesosphere. This means that sodium atoms in the mesosphere at these latitudes, precessing about the magnetic field lines, are aligned relatively close to horizontal as well.

It has been shown from simulations by Rampy et al., Fan et al., and the Rochester Scientific group[19, 34, 53] that an ideal resonance signal is observed when the laser beam is at right angles to the magnetic field lines. Decreasing the laser angle with the magnetic field lines, i. e.pointing the beam closer to parallel to the magnetic field, tends to increase overall sodium backscatter[52], but causes the Larmor resonance peak to become less prominent.

For this purpose, we will aim to maximize the laser beam launch angle to receive optimal resonance signal against the background scatter. It may be possible to exploit an entirely different transition and observe resonances within the sodium hyperfine structure, but this is an overall different experiment that requires further study, and will only be covered briefly in Chapter 7.

3.5 A BRIEF SUMMARY

Using the knowledge we have gained from LGS research, we can navigate the nuances involved in maximizing a return signal from a sodium laser upon the mesosphere. It is worth taking a few moments to summarize this knowledge before moving on to the section on our experimental methods, in order to elucidate our choices for the laser system.

Our experiment aims to measure return fluorescence from excited mesospheric sodium via laser light tuned to the sodium D_2 transition at $589\mathrm{nm}$. We will utilize circularly-polarized laser light to optically pump sodium above the lowest ground state, preventing the atoms from becoming lost to the excitation process and causing a decrease in overall fluorescence over time. With this in action, we aim to observe the resonant increase in sodium backscatter above background levels by pulsing the laser beam at a rate equal to the naturally-occurring Larmor precessional frequency caused by the ambient geomagnetic field. We will achieve this by sweeping the laser pulse frequency and recording return scatter at each PRF. The pulse frequency at which sodium fluorescence is at a maximum is equal to the natural Larmor frequency of sodium in the mesosphere, and this value is proportional to the magnetic field strength.

Since our experiment takes place at polar latitudes, we expect to have less-than-ideal resonance signal against the background non-resonant fluorescence. We will accommodate this as best we can by maximizing the laser beam angle with the magnetic field lines.

With this understanding, we can now proceed to a discussion of our experimental system.

Part II

METHODS FOR EXPERIMENT AND MODELING

With an introduction to the underlying physical concepts behind remote laser magnetometry, this section will focus on experimental setup. This includes hardware specs for the lasers as well as environmental factors. This section will also detail the content of the LGSBloch package for Mathematica, used for simulating our expected results.

4

EXPERIMENTAL SYSTEM

4.1 ENVIRONMENTAL PARAMETERS

ALOMAR lidar observatory is located in Andenes, Norway, 300 km north of the Arctic circle at $69°16'\mathrm{N}, 16°00'\mathrm{E}$[18].

Before continuing on to discuss modeling of our experiment, it is important to summarize relevant input parameters that correspond to the environment at ALOMAR. These are contained in Table 1. Sodium column and number densities are taken from Tim Dunker, as well as the value for atmospheric transmission, wintertime sodium centroid altitude, and temperature values[17, 18].

Table 1: Environmental Parameters at ALOMAR

Parameter	Value
Telescope Altitude above sea level	380m
Altitude of measurement	$80 - 100\mathrm{km}$
Magnetic field strength	$\approx 50990\mathrm{nT}(0.51\mathrm{G})$
Magnetic declination	$6.2°$
Magnetic inclination	$77.8°$
Na column density (winter)	$2 \times 10^{13}\mathrm{m}^{-2}$
Na number density (winter)	$2 \times 10^{9}\mathrm{m}^{-3}$
Temperature	$180 - 220\mathrm{K}$
Atmospheric transmission	$0.9 - 0.98$
Sodium centroid altitude	$90\mathrm{km}$ (winter)
Laser beam angle to magnetic field	$168.14°$
Telescope (detector) diameter	$1.8\mathrm{m}(\times 2)$

Magnetic field strength and orientation were determined for Andenes, Norway at $90\mathrm{km}$ altitude using the IGRF calculator at the NOAA (National Oceanic and Atmospheric Association) website [47]. Declination refers to the angle between true North and magnetic North. Inclination is the angle between the magnetic field vector and the horizontal plane at $90\mathrm{km}$.

The laser beam angle in Table 1 is given as $168.14°$, which is calculated from zenith at Andenes compared to magnetic field lines. This angle is defined with the magnetic field lines pointing downward in the northern hemisphere. This means that the laser beam makes an angle of $11.86°$ from the vertical z-axis defined along the field lines, but the directional distinction is important for the LGSBloch package, to ensure functionality of the program.

4.2 CURRENT TOPTICA LASER

Figure 22 is a schematic showing the current laser system at ALOMAR observatory. Each part will be discussed in detail below, with yellow denoting components that make up the actual Toptica laser-generating system, and blue denoting external components.

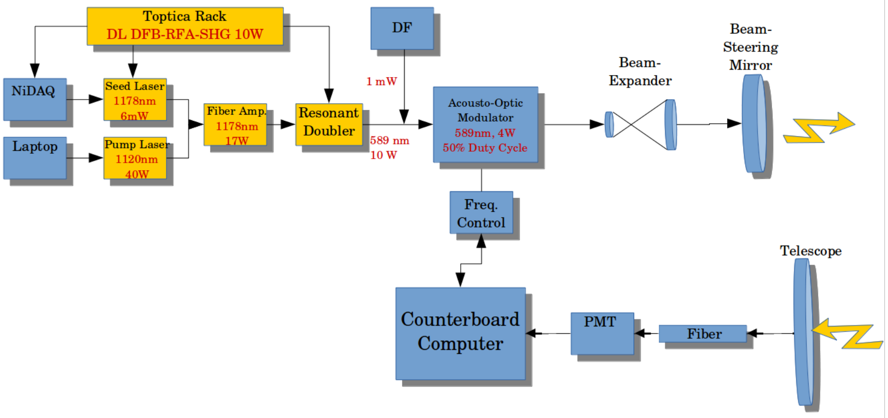

Figure 22: Current laser setup at ALOMAR

Currently at ALOMAR there is a Toptica DL DFB-RFA-SHG 10W CW laser. The following acronym breakdown and description is taken from the Toptica spec sheets[58].

DL DFB classifies the Toptica as a Diode Laser, specifically, a Distributed FeedBack Diode Laser. This means that, instead of using two discrete mirrors to form the laser's optical cavity, there is instead a one-dimensional interference grating providing the optical feedback.

RFA describes the type of amplification within the laser, a Raman Fiber Amplifier. This means that the signal is intensified via Raman amplification within an optical fiber, using stimulated Raman scattering processes.

SHG describes the doubling stage of the laser, the Second-Harmonic Generator. Physically, it is a folded ring cavity in bow-tie configuration, with excellent thermal and mechanical stability[58].

As the next letters perhaps obviously suggest, the laser has an output of approximately $10W$, and is a Continuous Wave or Continuous Waveform (*CW*) laser. The term "continuous wave" here refers to the constant amplitude and wavelength of the electromagnetic wave. The laser itself continuously emits light. This in no way refers to the pulsing, or lack thereof, of the beam, which we control with an external pulse generator and acousto-optic modulator (described in detail in following subsections).

Table 2 summarizes the laser parameters of the current Toptica laser at ALOMAR.

Table 2: Toptica Laser Parameters

Parameter	Value
General	
Laser wavelength	$589.159nm$
Laser output power	$10W$
Laser polarization	linear/circular
Laser linewidth	$< 500kHz$
Beam width (after AOM)	$1-2mm$
Receiver baseline	$\approx 5m$

Looking at Figure 22, we now know the essentials of what is contained within the box labeled "Toptica Rack", including th seed and pump laser, fiber amplifier, and resonant doubler. Let's look at the rest of this schematic.

4.2.1 *Beam Modulation*

There are two components that come into play when we consider pulsing the laser beam. First is a waveform generator, or frequency controller as labeled in Figure 22, with which we can set and adjust the pulse frequency and duty cycle. Second is the acousto-optic modulator (AOM), which drives the beam according to the signal defined by the pulse generator.

Our waveform generator is a Berkeley Nucleonics Corporation (BNC) model 645, capable of generating pulses up to $10MHz$, with variable duty cycle and minimum pulse width of $20ns$[15]. This suits our needs of $\approx 600ns$ pulses at a pulse frequency of $300-400kHz$.

Via the front panel or remote (computer) control, we can vary the period, pulse width, and amplitude of our desired signal.

The BNC controls the AOM driver. The Acousto-Optic Modulator (AOM) uses sound waves to diffract and shift the frequency of light. The oscillating electric signal from the waveform generator drives a piezoelectric transducer to vibrate, creating the sound waves whose intensity in turn modulates the intensity of the light beam[1].

At ALOMAR, there is a Brimrose FGM-80-2-589 Acousto-Optic Modulator, with Brimrose FFA-80-B2-F2.5 80MHz Fixed Frequency Driver. The AOM is centered on sodium D_2 wavelength of $589nm$, capable of pulsing at $80MHz$ with a 0.015% frequency accuracy and $190s$ risetime.

4.2.2 *Beam Collimation & Beam Steering*

Since laser magnetometry endeavors to maximize the amount of return fluorescence from the mesosphere, it is reasonable to also optimize the intensity of available laser light to induce as much sodium backscatter as possible. This can be controlled by beam collimation and the use of a beam-expanding telescope.

Beam collimation is the process of minimizing the divergence of a given beam of light, i. e., focusing the beam at infinity. A shear plate or shearing interferometer can be used as a collimation test device, consisting of a wedged optical flat mounted at 45° and diffuser plate with a ruled reference line down the middle. The diffuser plate is designed to view interference fringes created by Fresnel reflections from the front and back surfaces. If the beam is collimated, the fringe pattern will be parallel to the reference line, as shown in Figure 23.

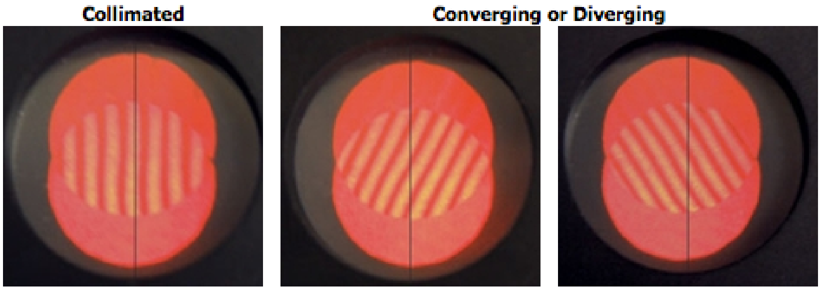

Figure 23: Shearing interferometer diffuser plate, from ThorLabs[60].

We currently have a Thorlabs SI500 shear plate for $25-50mm$ beam diameters[60].

Beam expanders can then take collimated light and expand or reduce its size. These include both refractive and reflective telescopes, though a Galilean telescope is commonly used[35].

At ALOMAR, after beam expansion, the laser is usually split and directed to the beam-steering units. In order to maximize laser power, we will not split the beam, and instead direct the laser beam from units which are mounted about $3m$ off the telescope axis, as shown below in Figure 24. Increasing this baseline distance helps mitigate interference from Rayleigh backscatter.

4.2.3 *Receiver*

The outgoing laser light is emitted along the optical axis of the receiving telescopes. There are two Cassegrain telescope receivers located at ALOMAR, called the North-West Telescope (NWT) and South-East Telescope (SET), since both are independently tiltable to 30° off-zenith, respectively to the northwest and southeast quadrant. Each telescope has a primary mirror with diameter $1.8\mathrm{m}$ and a field of view of $180\mu\mathrm{rad}$[31].

Figure 24 illustrates the setup of the telescope hall at ALOMAR, with the sodium laser beam represented in yellow.

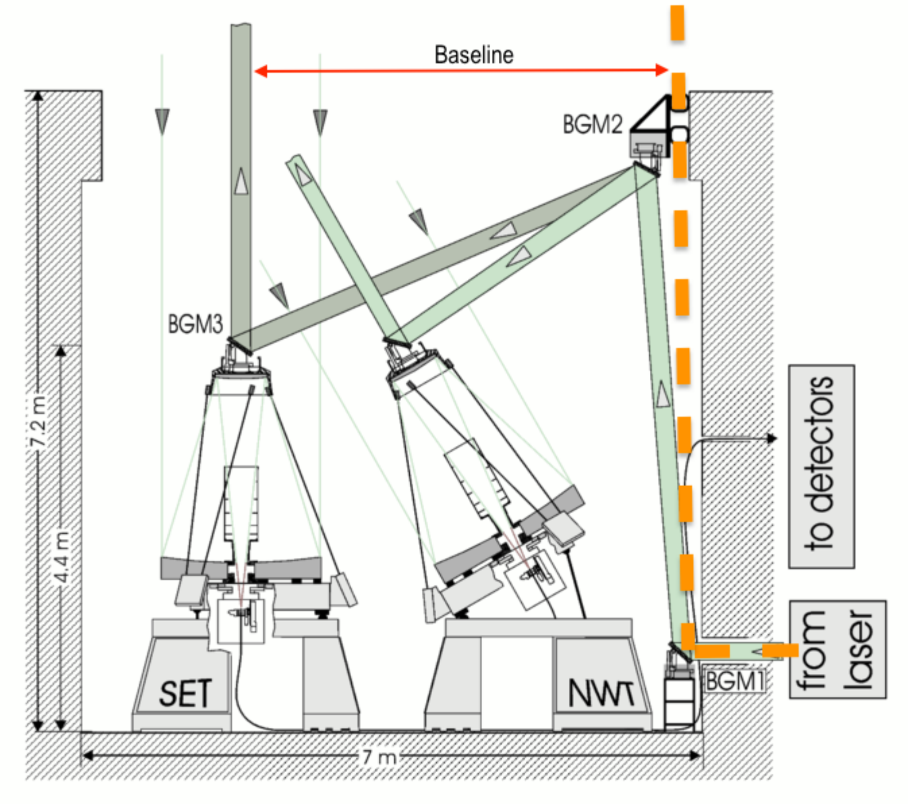

Figure 24: Setup of the South-East Telescope (SET) and North-West Telescope (NWT) in the telescope hall at ALOMAR observatory. Figure from Institut für Atmosphärenphysik (IAP)[37].

For comparison to normal operations, the pale green lines demonstrate the positioning of the RMR lidar, split into two and directed to the beam steering mirrors along the optical axis at the top of each telescope. In order to minimize interference from Rayleigh backscatter, we will maximize our baseline by launching the laser beam through a separate hole from the RMR lidar, and using the SET as our receiver and projecting the sodium laser beam at a distance. This is for the case observing at zenith.

Backscattered photons hit the receiver primary mirror, and are reflected onto a secondary mirror located at the top of the telescopes. The photons are then directed to the primary focus and, via a collimating lens, to a multimode fiber entrance[17]. Since the telescopes are shared with the ALOMAR RMR lidar, there are three fibers connected to the base of each telescope, two for the RMR lidar at the focal point, and one currently attached for the sodium system, slightly off-focus. The multimode fiber for the sodium laser has a numerical aperture of $NA = 0.39$ and a diameter of $d = 1.5mm$.

Collected light is transported via the fibers, with lengths of $7m$ for NWT and $11.7m$ for SET[17]. The fibers guide the collected backscattered light to the optical bench, passing a collimating lens ($f = 25.4mm$) and an interference filter. For measurements in darkness, this filter has a transmission window centered at $589nm$, with a bandwidth of $1nm$. In this way, the majority of photons that do not originate from sodium resonance fluorescence are blocked, such as starlight, moonlight, or aurora. For daytime measurements, a FADOF (Faraday Anomalous Dispersion Optical Fiber) is used to suppress solar background by a factor of 2×10^5[13]. The FADOF passband is so small that is must be measured daily, with the filter curve included in analysis.

After filtering, the photons are then detected by the photocathode of a Hamamatsu R932-02 photomultiplier tube (PMT)[17]. The photon counts are then stored to disk.

4.3 FASOR FROM KANE ET AL.

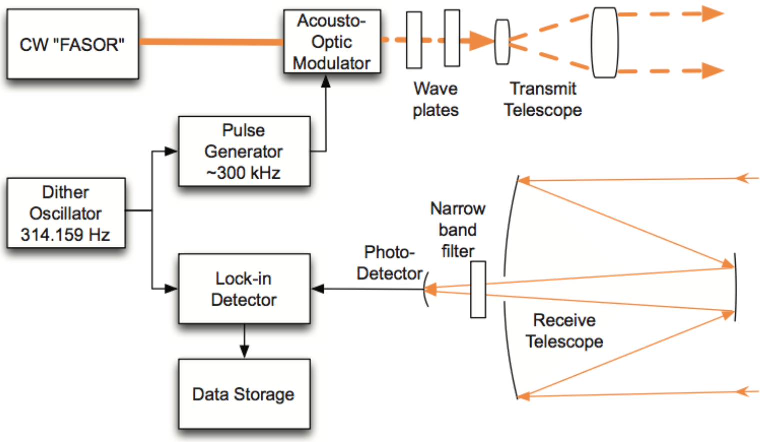

Figure 25: Diagram of Kane et al. experimental system [42].

The light source used by Kane et al.[42] was constructed as a prototype laser guidestar system. It functions very similarly to the Toptica system, combining the 1064nm and 1319nm wavelengths of a Nd:YAG solid state laser in a resonant cavity to produce an output of 589nm. Their configuration is called a FASOR, for Frequency Addition Source of Optical Radiation[44].

It is unfortunate that the current 10W laser system at ALOMAR will eventually be moved back to the United States. The fortunate follow-up to this, however, is that we have the possibility to borrow the FASOR used in the recent Kane et al. paper. I will refer to this laser as the "Kane laser" to prevent confusion with the information in the previous section.

A schematic of the Kane laser is shown in Figure 25. The full optical bench of the Kane laser is visualized in Figure 26. These parameters of the full laser component fit the available optical table at ALOMAR.

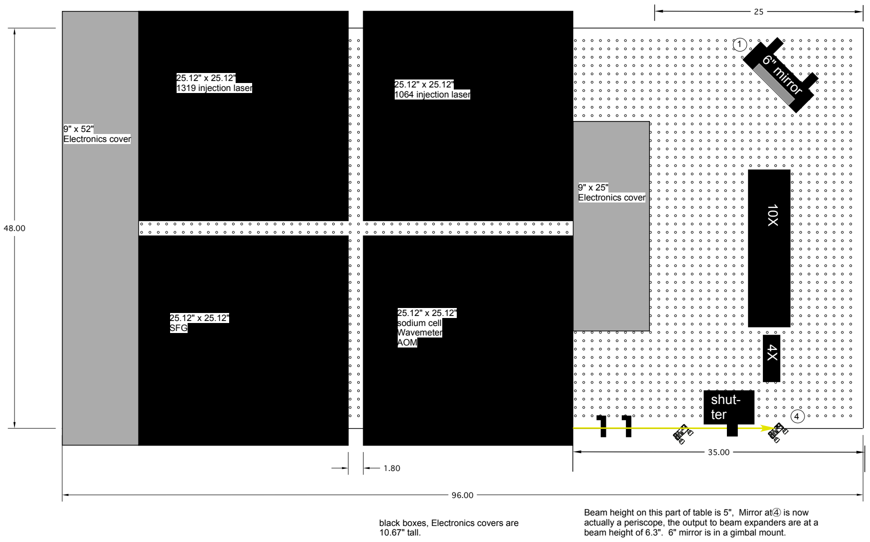

Figure 26: Kane laser optical bench, with all laser components laid out. This schematic was sent by Paul Hillman from Kane et al.

Paul Hillman and Craig Denman note that, in addition to the components of the optical table, there is a full-size 19-inch rack of electronics, a short (2.5-foot high) 19-inch rack with diode power supplies (120V, 20A × 2), and a water chiller that takes 208V, single phase. Given the already-existing laser infrastructure at ALOMAR, these should be easily accommodated.

Parameters of the Kane laser are detailed in Table 6 and in the following subsection. In the final section, I will compare this with the current Toptica system.

Table 3: Kane et al. FASOR Parameters

Parameter	Value
General	
Laser wavelength	$589.159\mathrm{nm}$
Laser polarization	circular
Laser linewidth	≈ 0
Laser output power	$10 - 20W$
Duty Cycle	20% and 35%

4.3.1 *Kane Laser Parameters*

Like the Toptica laser, this continuous waveform, single-frequency FASOR generates light at $589.159\mathrm{nm}$ by frequency summing the output of two lasers, a $1319\mathrm{nm}$ and a $1064\mathrm{nm}$ single-frequency source. The output is $10W$, but the output has been able to reach $20W$ [4].

The light is then also passed through an AOM, model Gooch & Housego 35085-3. The polarization state of the beam output from the AOM can then be adjusted to any arbitrary state with the use of a quarter waveplate and a half waveplate in combination [42].

Simulations of their setup, run with the same LGSBloch program that we have used, had an optimal duty cycle of 20%, but experimentally, they found optimum performance at 35% duty cycle.

A beam-expanding telescope and shear plate were also used by Kane et al. to optimize collimation of the light.

4.4 COMPARISON OF LASER SYSTEMS

Though there is the possibility of reaching power outputs of $20W$ with the Kane laser, on average, the two lasers have comparable output laser power. Aside from this difference, the most important parameter to contrast between these two lasers is the linewidth.

Laser linewidth refers to the statistical "spread" of light frequency in the beam. This is generally a Lorentzian function, with the linewidth referring to the FWHM of this function. I. e., instead of 100% of the laser light tuned precisely to the sodium transition, a wider bandwidth includes a small percentage tuned to just above and just below the transition wavelength.

Both the Kane laser and Toptica laser have very small linewidth; Kane et al. modeled their system in Kane et al. [42] with an effective linewidth of 0Hz. The Toptica laser spec sheet lists a linewidth of < 500kHz[58].

For laser magnetometry, it is actually an improvement to use a broader linewidth. Since the sodium atoms in the mesosphere are not stationary, different velocities of these atoms will lead to a Doppler broadening of the sodium resonance transition. A laser with a linewidth roughly equal to the Doppler-broadened sodium linewidth, around 500MHz, will interact with all of the sodium atoms instead of only those of one velocity class [42].

Recalling Figure 17 from the atomic physics chapter, we can imagine another benefit of wider laser linewidth. A linewidth with a span of approximately 2GHz eliminates the need for repumping, since a percentage of the laser light will already excite some of the $\mathbf{F} = 1$ transition, and there is no need to manually tune the laser for repumping[52].

Having a narrow-linewidth laser may have the ability to resolve hyperfine transitions, which is an experiment also proposed by Higbie et al.[29]. This is discussed further in Chapter 7.

With a full, quantitative description of our environmental parameters and two potential laser probes, we can now proceed to a discussion of simulation techniques for remote magnetometry measurements.

5

MODELING

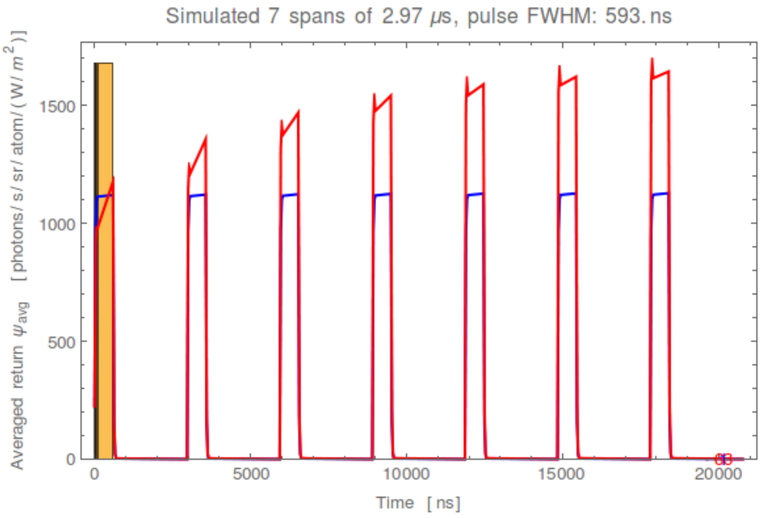

Figure 27: Simulated pulse train used in LGSBloch models.

The primary purpose of modeling is to make an attempt at answering some vital questions about our experiment. Namely, given fundamental differences in environmental parameters and laser geometry, how effective is this method? Can we expect results that will make laser magnetometry even plausible? To help answer these questions, we made use of the LGSBloch program, a part of the Atomic Density Matrix (ADM) package for Mathematica, and developed by Simon Rochester and Ron Holzlöhner.

It is available online at http://rochesterscientific.com/ADM/[54].

With this package, we were able to simulate a pulsed laser beam incident on the sodium layer at 90 km, in an environment similar to that at ALOMAR observatory. Figure 27 is a visual representation of our laser pulse train, and will be discussed further in Section 5.1.4.

5.1 LGSBLOCH AND SIMULATIONS

The LGSBloch package models the sodium-light interactions by calculating density matrices using the phenomenological optical Bloch equations[34]. The density matrix then describes the statistical state and evolution of an ensemble of atoms with user-specified parameters[6].

Much of the mathematical breakdown of atomic evolution is adapted from Rachel Rampy and Ron Holzlöhner[33, 52].

5.1.1 *The Mathematics of LGSBloch*

The evolution of atoms can be modeled using the optical Bloch equations for the atomic density matrix. This describes the statistical state of an ensemble of atoms. The evolution of the density matrix, ρ, is given by a generalization of the Schrödinger equation:

$$\frac{d}{dt}\rho = \frac{1}{i\hbar}[H, \rho] + \Lambda(\rho) + \beta \tag{8}$$

where H is the total Hamiltonian, $\Lambda(\rho)$ accounts for any additional relaxation processes of the atom, and β includes the entrance of new atoms into the beam, which are independent of ρ. Let's break down these terms.

The Hamiltonian describes the interaction between the atomic energy structure with any external fields. H is a combination of terms,

$$H = H_0 + H_E + H_B \tag{9}$$

It includes the Hamiltonian of the unperturbed atom(H_0), that of the interaction of the atom's electric dipole with the electric field of the incident light ($H_E = -d \cdot E$), and that of the interaction of the magnetic moment of the atom with the local magnetic field ($H_B = -\mu \cdot B$). The use of square brackets in Equation 8 denotes the commutator.

$\Lambda(\rho)$ may account for many relaxation processes, such as spontaneous decay, collisional spin-relaxation, or the loss of atoms due to motion out of the beam (or motion of the beam away from the atom). $\Lambda(\rho)$ also describes changes in velocity of the atoms due to collisions and light-induced recoil.

For each relaxation process, there is a corresponding repopulation, due to conservation of the total number of atoms (no new atoms are being spontaneously created or destroyed). This repopulation is contained within the term β.

5.1.2 *Solutions to Schrödinger Equation*

Solutions to Equation 8 give a linear system of differential equations for the density matrix elements, known as the optical Bloch equations[33].

We can then think of ρ as a column vector of the density matrix elements, containing 576 (24×24) states of the sodium ensemble for each velocity class. The Bloch equation system that describes the sodium D_2 excitation in the mesosphere can then be written as

$$\dot{\rho} = \mathbf{A}\rho + b \tag{10}$$

The vector b corresponds to the β term in Equation 8, and the matrix $\mathbf{A}$ to the remaining terms on the right hand side.

In practice, the Bloch matrix $\mathbf{A}$ depends, among many other parameters, on the laser irradiance on the mesosphere, percentage of laser frequency tuned to D_{2a} and D_{2b}, and the polarization incident on the atoms [33]. These parameters will be unpacked further in Section 5.2.

Through LGSBloch, the linear system is solved by implementing a method built into Mathematica. The fluorescent photon flux per solid angle emitted in a given direction can be found from the steady-state solution for ρ as the expectation value of a fluorescence operator [14, 34].

In order to account for non-uniform irradiance on the mesosphere, the LGSBloch package uses a Gaussian intensity distribution, with user-defined FWHM and irradiance level

5.1.3 *Velocity Groups*

To describe atoms with different Doppler shifts, the velocity dependence of ρ is discretized. We assign a fixed number n_{vg} of velocity groups, each with a fixed longitudinal velocity. The complete density matrix ρ can then be thought of as n_{vg} separate, but coupled, density matrices, each with dimension 24×24, corresponding to the 24 magnetic substates of the D_2 transition. This is possible because we can neglect coherences between atoms that have different velocities[53].

The number of calculated velocity groups corresponds to the "spread" of the resonance peak, as sodium atoms in motion will emit fluorescence Doppler shifted from the Larmor frequency. This will become relevant for discussion of our simulation results, and will be considered further in Chapter 7.

5.1.4 *Simulating a Pulsed Laser*

Simulations of a pulsed laser beam on the mesosphere were carried out using the `StepPulseFlux[]` routine in LGSBloch. `StepPulseFlux[]` approximates pulses using a piecewise constant function, then solving the function using iterative sparse matrix exponential routines that do not diverge[33].

The evolution equation for each step is taken to have constant coefficients, with the solution given by Equation 11:

$$\rho(t+\Delta t) = (\rho(t) - \rho_{ss})\exp(\Delta t\mathbf{A}) + \rho_{ss}, \qquad \mathbf{A}\rho_{ss} + b = 0 \tag{11}$$

where the function $exp()$ denotes the matrix exponential (as opposed to a matrix *of* exponentials), and ρ_{ss} denotes the steady state matrix. The condition on the right is satisfied for continuous waveform (cw) lasers[33]. Mathematica employs a package which solves Equation 11 without computing the matrix $exp(\Delta t\mathbf{A})$ explicitly. This is the approach used in the `StepPulseFlux[]` routine.

Each simulation produced a plot demonstrating the pulse format for the indicated PRF and duty cycle. An example of this can be seen in Figure 27, which shows a 7-pulse train at 337 kHz and 20% duty cycle. The two colors represent two separate levels of mesospheric irradiance, with the blue at an average $0.07W/m^2$ and the red averaged at $12.4W/m^2$.

Separate mesospheric irradiance levels are calculated automatically by the program to compare laser efficiency formats, but is not relevant for our purposes calculating average return flux from a user-defined mesospheric spot size.

5.1.5 *Value of Average Return Flux*

For all the simulations presented in Chapter 6, we ran the program at given parameters and pulled values using the program-calculated average return flux on the ground, Φ, measured in units of $photons/s/m^2$:

$$\Phi = \frac{C_{Na} X T_a{}^X F_m}{L^2} \tag{12}$$

with C_{Na} as the sodium column density ($atoms/m^2$), X is the airmass at given zenith angle, T_a is the one-way transmission of the atmosphere, L is the line-of-sight distance between the launch telescope and the sodium layer, and F_m is an expression of the emitted photons from the sodium layer integrated over the receiver area orthogonal to the beam A, subtending the solid angle A/L. Equation 12, the average return photon flux at the detector, is given by Ron Holzlöhner in [34]. This quantity is independent of irradiance level.

5.2 MODELING OUR OBSERVATORY ENVIRONMENT

5.2.1 *Simulation Input Parameters*

Each run of the LGSBloch simulation is based on an ascii file containing the relevant parameters. Table 4 shows the input parameters for the simulation modeling our laser system, with f standing in as the variable pulse frequency value, which was changed for each simulation run. The range of pulse frequency values were taken to range ± 10kHz around the anticipated Larmor frequency (or resonance frequency) value, in increments of 1kHz.

Table 4: LGSBloch Input Parameters

Input (`params.txt`)	Description	Value
	Pulse Parameters	
`tPulse`	FWHM pulse duration [s]	$0.2 \times (1/f)$
`trepMicro`	Micro pulse rep time [s]	`tPulse`/0.2
`magZenithDeg`	Laser angle to field lines [deg]	168.18
`ΔfLaserFunction`	Laser central frequency offset [Hz]	0
`FWHMmeso`	Mesospheric beam FWHM [m]	0.8
`iMesoStepN`	Irradiance levels to compute	2-5
`nPeriods`	Micro pulse periods to simulate	7
	Parameters of `PsiMeso[]`	
`PLaunch`	Laser launch power [W]	10.0
`Htele`	Launch height above sea level [m]	380.0
`Ta`	Atmospheric Transmission	0.9
`RepumpFraction`	amount of light tuned to D_{2B}	0.2
`LightPolarization`	Laser polarization state	0 and 1
`BG`	Magnetic Field Strength [G]	0.5099
`FWHMbw`	Laser FWHM bandwidth [Hz]	4×10^5
	Calculated Larmor frequency = 356.8kHz	

Simulations were run for the case of both linear and circular polarization. `LightPolarization` is defined as the ellipticity angle, with 0 corresponding to linearly polarized light and 1 to circularly polarized light.

The factor of 0.2 in `tPulse` and `trepMicro` is included to maintain a constant duty cycle of 20% while running simulations at different pulse repetition frequencies. This made it easier to adjust the value of f only once for each run.

Part III

RESULTS AND DISCUSSION

This section presents all initial simulation results. This includes test attempts to recreate the numerical results of Higbie et al. and model the experimental Kane et al. results. Finally, I conclude with a discussion of these first simulations and considerations for subsequent modeling attempts.

6

SIMULATION RESULTS

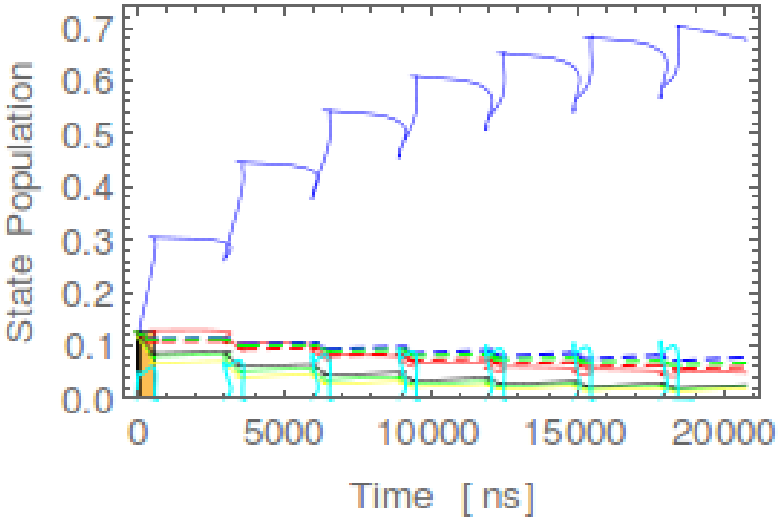

Figure 28: Plots showing the evolution of total ground and excited state populations at an irradiance level of $0.07W/m^2$. Solid blue: (F=2, m=+2), solid red: (F=2, m=+1), solid green: (F=2, m=0), solid yellow: (F=2, m=-1), solid black: (F=2,m=-2), dashed blue: (F=1,m=+1), dashed red: (F=1,m=0), dashed green: (F=1,m=-1).

To model our system, we ran the pulsed laser `SimPulsedShow` and `SimPulsedLGSParallel` programs written by Ron Holzlöhner, which provides simulation plots of the user-defined pulse format, average and specific return flux values, and atomic state populations.

Figure 28 is taken directly from the program output, and demonstrates very nicely the atomic physics covered in Chapter 3. We can see that for a circularly polarized laser system pulsed at a 20% duty cycle, atomic populations quickly orient toward the (F=2,m=+2) hyperfine state, as expected. The jaggedness of the curve follows the laser pulsation at 337kHz.

The first section will present attempts to replicate the Higbie and Kane plots, followed by resonance plots using environmental parameters at ALOMAR, using a similar method. In the final section of this chapter, I will present a mockup plot overlaying this sodium resonance on real magnetometer data taken during both magnetically active and quiet periods, to simulate actual measurements from a laser magnetometry experiment.

6.1 REPLICATIONS OF HIGBIE & KANE

In order to estimate the effectiveness of laser magnetometry, especially given the unusual placement at such a high latitude, we found it crucial to recreate Figure 2 and Figure 3 as closely as possible, inputing parameters from Higbie et al. and Kane et al. As a reminder, these plots show the peak of sodium backscatter at resonance between laser pulse frequencies and the sodium Larmor frequency.

These mockup plots were made using the LGSBloch package, with the `SimPulsedShow` and `SimPulsedLGSParallel` regimes written by Ron Holzlöhner for Mathematica. All return flux values were gathered by running the simulation and printing out values of Φ from the resulting plot.

6.1.1 *Higbie et al. Simulation Results*

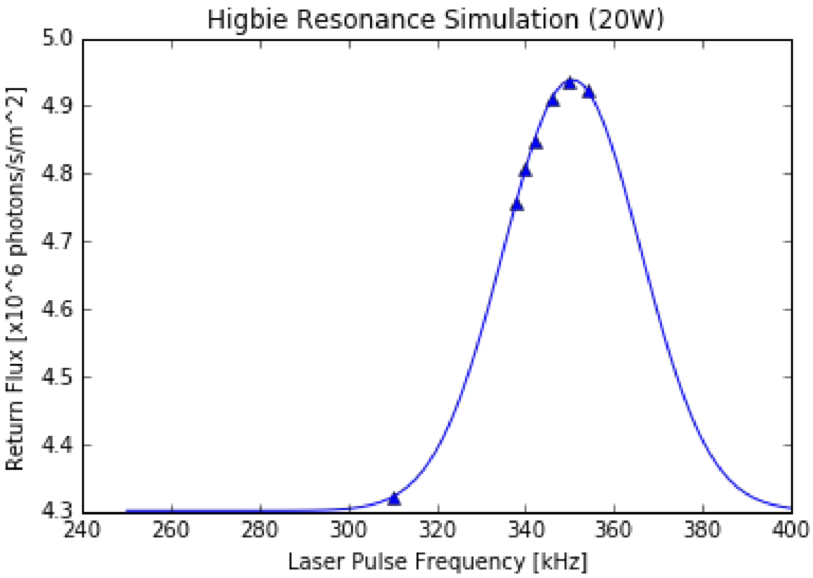

Figure 29: Recreation of sodium resonance backscatter plot from Higbie et al.[29], using LGSBloch package for Mathematica, with a Gaussian fit. This plot shows a peak at laser pulse frequency value of approximately 350kHz, as expected.

The parameters used to generate Figure 29 are taken directly, when possible, from [29]. Some parameters were not specified in the literature, such as `Ta`, atmospheric transmission, and `CNa`, sodium column density, and so were either estimated based on qualitative description (such as setting `Htele` as 0 when the paper assumes "on the ground") or left as our own values.

All parameters input into the `SimPulsedShow[]` and `SimPulsedLGSParallel` regimes are listed in Table 5.

Table 5: Higbie Mockup Input Parameters

Input (`params.txt`)	Description	Value
	Pulse Parameters	
`magZenithDeg`	Laser angle to field lines [deg]	90.0
`ΔfLaserFunction`	Laser central frequency offset [Hz]	0
`FWHMmeso`	Mesospheric beam FWHM [m]	0.8
`PLaunch`	Laser launch power [W]	20.0
`Htele`	Launch height above sea level [m]	0.0
`Ta`	Atmospheric Transmission	0.85
`RepumpFraction`	amount of laser light tuned to D_{2B}	0.2
`LightPolarization`	Laser polarization state	1
`BG`	Magnetic Field Strength [G]	0.5
`FWHMbw`	Laser FWHM bandwidth [Hz]	8×10^8
`CNa`	Sodium Column Density [m^{-2}]	2×10^{13}
	Calculated Larmor frequency = 350kHz	

Laser pulse frequency values were chosen by calculating the Larmor frequency value in the manner described in Section 3.2.3. As in the original paper, we calculate a Larmor frequency value of $f_L =$ 350kHz. Each plot point requires over an hour to compute, so a rough outline was made with plot point values in steps of 4kHz.

Figure 29 confirms the presence of a resonance peak at $f_L =$ 350kHz. The percentage increase in return flux is also comparable, around 15%, though the width of the resonance peak is much wider than that shown in Higbie et al. Unlike Figure 2, however, the curve does not "flatten out" away from the resonance peak. This will be discussed further in Chapter 7.

6.1.2 *Kane et al. Simulation Results*

The experimental results given in Kane et al.[42] exhibit a different shape than those modeled by Higbie et al., and were fit with a triangle function instead of a Lorentzian. Kane's measurements slowly decrease from the peak, without bottoming out at a constant "background" fluorescence as shown in Higbie.

Figure 30 shows our model of the resonance peak measured by Kane et al., with parameters listed in Table 6.

There are several differences between our simulation and Kane's results. The percentage of increase in the resonance peak is much smaller than what they were able to measure; Figure 3 gives an in-

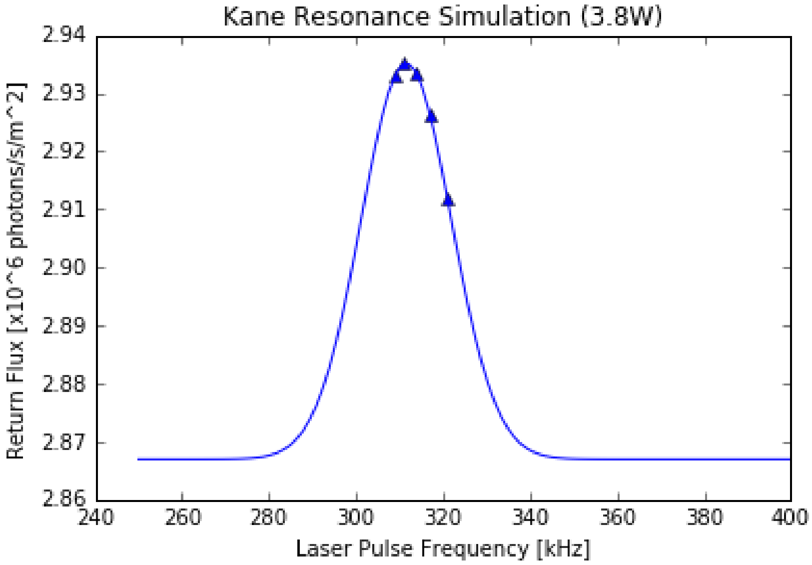

Figure 30: Recreation of sodium resonance backscatter plot from Kane et al.[42], using LGSBloch package for Mathematica and a Gaussian fit. Resonance Peak is at approximately PRF = 313kHz, ≈ 4kHz below calculated value.

crease close to 6% while simulations show closer to 3%. Data points for this plot are taken as unreliable, since it is fit to so few points. The most important consideration, however, is that the PRF at which resonance occurs is shifted down from the expected value of 317kHz to 313kHz.

This shift was also present in simulations done for ALOMAR, covered in the following section. Since the position of the resonance peak is critical in this experiment, this warrants full discussion and understanding. It is unlikely that it is an unconsidered physical phenomenon, as Kane et al. were able to measure their peak in the expected position.

This peak shift also occurs in our ALOMAR simulations, contained in the following section. It is present for any simulations made at laser angles other than 90°, and may be an issue with input parameters into the program.

This will be discussed further in Chapter 7.

6.2 ALOMAR SIMULATION RESULTS

The following results were modeled using the environmental conditions at ALOMAR observatory and the parameters for the current Toptica laser system, as detailed in the previous chapter in Table 4.

Table 6: Kane Mockup Input Parameters

Input (`params.txt`)	Description	Value
	Pulse Parameters	
`magZenithDeg`	Laser angle to field lines [deg]	60.0
`Zenith`	Beam angle from zenith [rad]	$30\pi/180$
`FWHMmeso`	Mesospheric beam FWHM [m]	0.8
`PLaunch`	Laser launch power [W]	3.8
`Htele`	Launch height above sea level [m]	2791.0
`Ta`	Atmospheric Transmission	0.84
`LightPolarization`	Laser polarization state	1
`BG`	Magnetic Field Strength [G]	0.453
`FWHMbw`	Laser FWHM bandwidth [Hz]	0
`CNa`	Sodium Column Density [m^{-2}]	4×10^{13}
(Duty Cycle)	Duty Cycle	0.35
	Calculated Larmor frequency = 317kHz	

6.2.1 *Long Plots*

Prior to making any individual point measurements for ALOMAR parameters, I ran two "long plots" to establish the rise time of scatter, and the long-term progression for circularly and linearly polarized laser light. The program ran over 39 pulses, and took over 10 hours for each simulation to run.

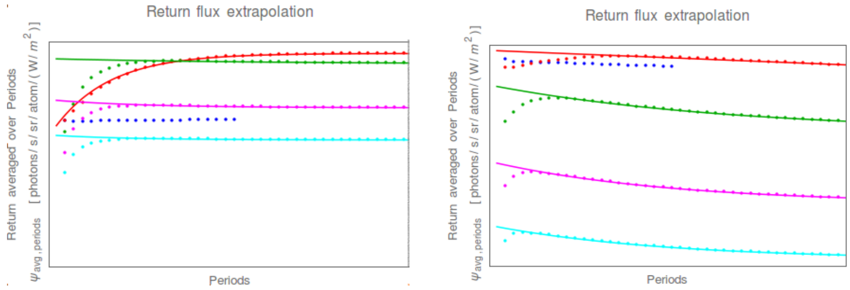

(a) Circular Polarization (b) Linear Polarization

Figure 31: Extrapolation of return flux over 39 pulses each, for circularly and linearly polarized laser light.

We can see from Figure 31 that it takes approximately $7-10$ pulses before the sodium atoms are pumped into a state that scatters stably. For the following single-point return values, I set the program to simulate 8 laser pulses in order to approximate a more realistic value of the return.

More importantly, we can see the long-term effects of circularly and linearly polarized laser light on the sodium return scatter. It was discussed in Section 3.3.2 that linearly polarized laser light does not pump sodium up from the lowest energy ground state, and that over time, sodium atoms would theoretically accumulate in this ground state and eventually become nonabsorbent to the incident light. Figure 31 supports this, as we can see a steady decline in return scatter for linearly polarized light, and observe a stabilizing constant return scatter for circularly polarized light.

6.2.2 *ALOMAR Resonance Peak Simulation Results*

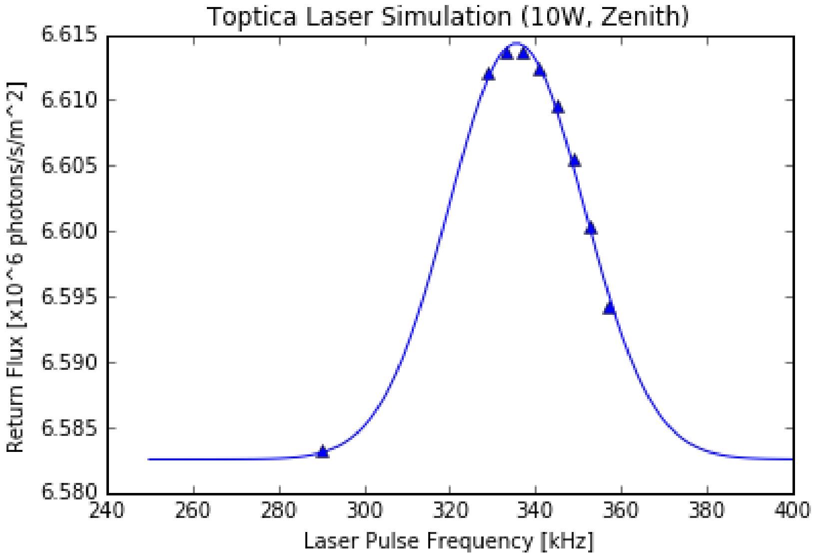

Figure 32: A plot of simulated return backscatter, for Toptica laser parameters as given in Table 4 with a Gaussian fit. The resonance peak appears at approximately PRF = 335kHz, about 22kHz below calculated value.

For early simulation attempts, it was necessary to run several "quick and dirty" plots with slight changes to parameters in order to observe any differences. Similar to Figure 29 and Figure 30 in the above sections, these were taken with plot points spaced 4kHz apart to gauge the general curve.

Figure 32 shows that a resonance peak is indeed present, though the percentage of increased return is incredibly small, around 0.5%. It is possible that this is a function of such a steep laser angle in reference to the external magnetic field, which we expected to yield a poor signal-to-noise ratio for resonance backscatter. This will be explored further in the following subsections, where we experiment with tilting the laser beam at wider angles from the magnetic field.

Like with Figure 30, the resonance peak appears shifted approximately 22kHz from the expected value at 357kHz. Since this occurred for the two plots made at non-orthogonal angles to the magnetic field, my suspicion is that it may be either incorrect input of the laser angle into the `params` file, or that the LGSBloch regimes are computing an angular component of the magnetic field that I am unaware of.

I first explored this problem by experimentally running the ALOMAR simulations at right angles to the magnetic field lines.

6.2.3 *Perpendicular ALOMAR Simulation*

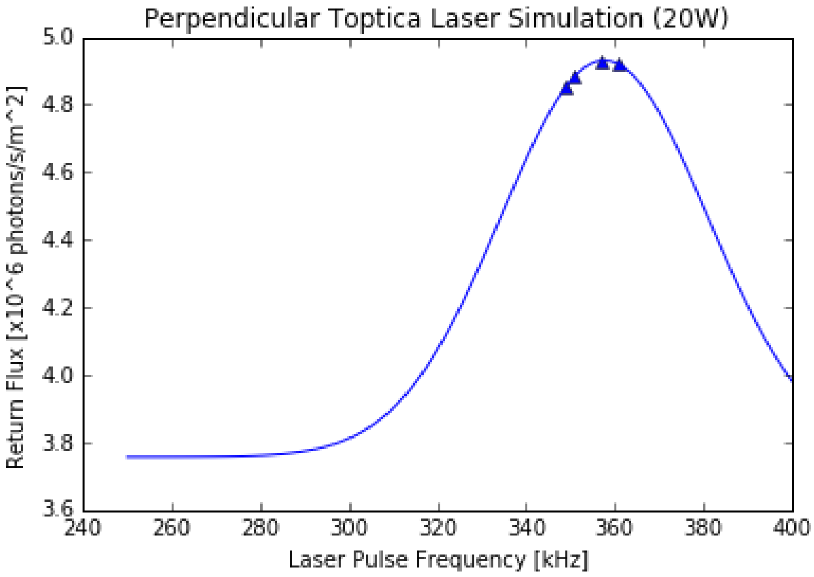

Figure 33: Simulation using parameters at ALOMAR observatory, laser power at 20W, but with laser beam angle set perpendicular to magnetic field lines. Resonance peak appears at the approximate calculated value of 357kHz.

All of the parameters remained the same as in Table 4 and Figure 32, with the exception of changing `magZenithDeg` to 90°, perpendicular to the surrounding magnetic field lines. The laser launch power was erroneously set to 20*W*, but is not greatly important for the purposes of this plot. Only a few plot points were taken to achieve a rough indication of the location of the resonance peak.

With these conditions, Figure 33 shows that the peak return flux does occur at the pulse frequency corresponding to the calculated Larmor frequency of 357kHz. Results from this plot on percentage of increased flux are unreliable due to the small number of simulated points.

This result supports the conclusion that the issue is with the input of the laser angle in the program. As mentioned at the beginning of this chapter, it is unlikely that this shift is due to an unexplored physical process, as Kane et al. physically measured this peak at the expected laser pulse frequency. Sorting out this issue is critical for creating accurate simulations of the experimental situation at ALOMAR observatory.

6.2.4 *Launch Telescopes Angled Off-Zenith*

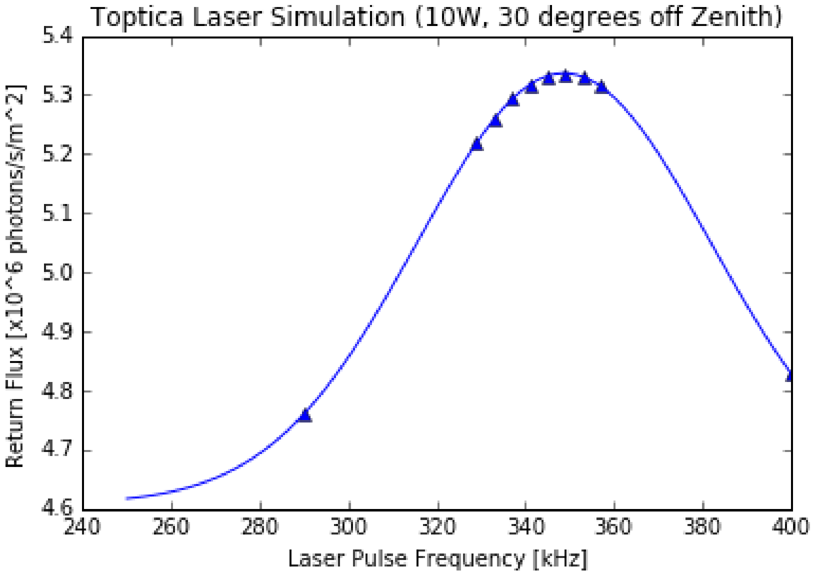

Figure 34: A plot of simulated return backscatter, for Toptica laser angled at 30° off-zenith, assumed northwards to maximize laser beam angle to magnetic field lines. Fit to a Gaussian.

Since LIDAR measurements made at ALOMAR observatory angle the launch mirrors off-zenith, it is possible that we can improve our resonance signal when the mirrors angle our laser beam at the widest angle with respect to the magnetic field.

Hildebrand et al.[31] describe the possible orientation of the launch telescopes at ALOMAR at up to 30° off zenith in any direction. If we assume this angle to be tilted north, we can estimate the return for a maximum laser beam angle to the magnetic field.

All parameters for Figure 34 are the same as Figure 32, except `Zenith` value was set to 30° to correspond with the laser beam launch angle from zenith, and `magZenithDeg` is therefore 138.14°. This angle shifts the latitude at which the mesosphere is illuminated, and thus the slight change in magnetic field strength was also taken into account for this new position, with `BG` set to 0.51G. This corresponds to a slight change in calculated Larmor Frequency, of 357.1 kHz.

We can see from Figure 34 that the resonance peak has crept closer to the calculated value, appearing at approximately $\mathtt{PRF} = 349\text{kHz}$.

This further supports that the issue is in the geometric calculations within the LGSBloch program.

An analysis of the resonance peak width and proportionality with the "floor" will follow in Chapter 7.

6.3 LONG-TERM MEASUREMENTS

The ultimate goal for the project is to take multiple magnetic measurements over the course of a night, in order to model the temporal fluctuations in field strength in the mesosphere.

Using magnetometer data from Tromsø Geophysical Observatory (TGO)[46], we can estimate the range of Larmor frequencies even during a particularly stormy night. This is demonstrated in Figure 35.

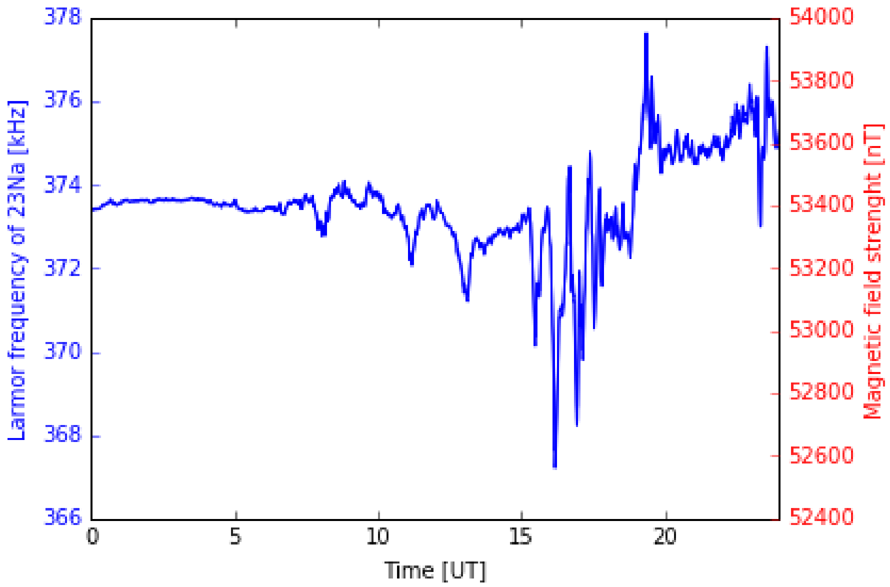

Figure 35: An example of a magnetically active night, and the range of sodium Larmor frequencies as a result. Magnetic Field data from October 16, 2016. Data from Tromsø Geophysical Observatory[46].

This and the following figures are based on ground based magnetometer data, assuming similar fluctuations at 90 km altitude. With this assumption, we can see from Figure 35 that even during an active event, the range of sodium Larmor frequencies is quite small. Each individual sweep of pulse frequencies can reasonably span $360 - 380$ kHz, so can easily take magnetic field measurements every second.

Using TGO data from a April 10, 2017 (a magnetically quiet night), January 3, 2017 (an average night) and October 16, 2016 (a stormy night), and a Lorentzian estimation of the resonance backscatter peak, Figure 36 – Figure 38 models the accumulation of a full 24-hours of magnetic field measurements using the laser magnetometry method.

We can consider this as a representation of the "raw" data, with the colorplot representing backscatter intensity with respect to the laser pulse frequency over time. From this, it is possible to then extract the maxima to produce a plot that resembles Figure 35, which can in turn be easily converted to a plot of magnetic field strength.

Figure 36 takes TGO data from a magnetically quiet day, with virtually no deviation from a background magnetic field value of 53, 400 nT, and overlays the Lorentzian curve of sodium resonance to model the backscatter at various laser pulse frequencies. The color corresponds to the proportion of increased backscatter at a given PRF, as given to the right of the plot.

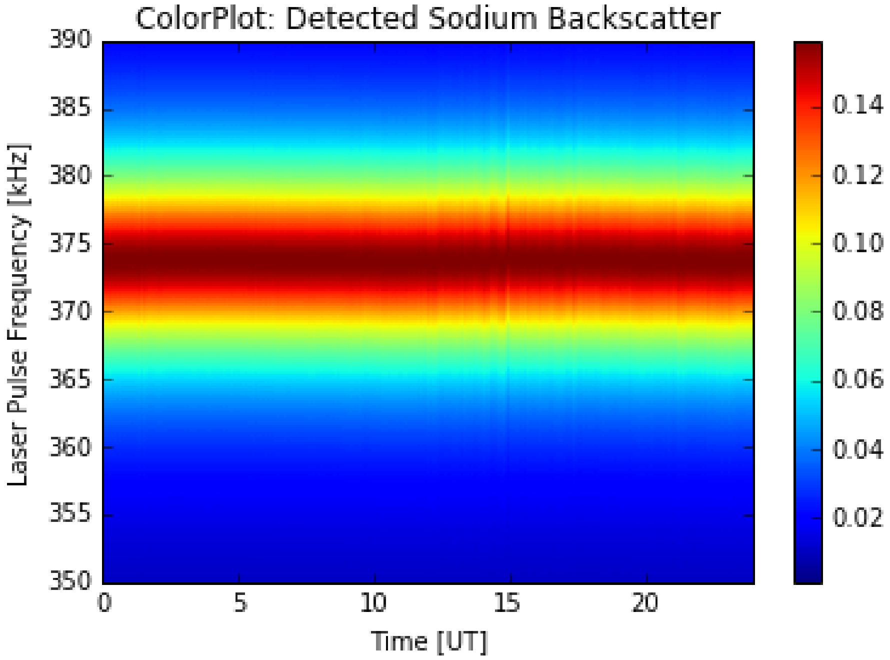

Figure 36: Mockup plost of detected backscatter as a function of laser pulse frequency over a 24-hour period, using magnetometer data from April 10, 2017, a day of relative magnetic quiet. Data from Tromsø Geophysical Observatory[46].

The peak width and proportion of increased backscatter in this and the following plots corresponds to the value calculated in the LGS-Bloch simulations for the Toptica laser at ALOMAR directed at 30° off zenith, as shown in Figure 34. This is the ideal situation, with largest resonance peak, for the observational environment at ALOMAR. The same Lorentzian curve is assumed for all points. Atomic fluctuations within the laser probe will change the width of our modeled curve, and one can surmise that the intensity of the resonance peak may also fluctuate with atmospheric conditions.

This quiet-day representation is presented to show the baseline spread of backscatter increase against a steady magnetic field.

It is common in later hours for there to be small substorms, or brief disturbances in the magnetic field, as shown in Figure 37.

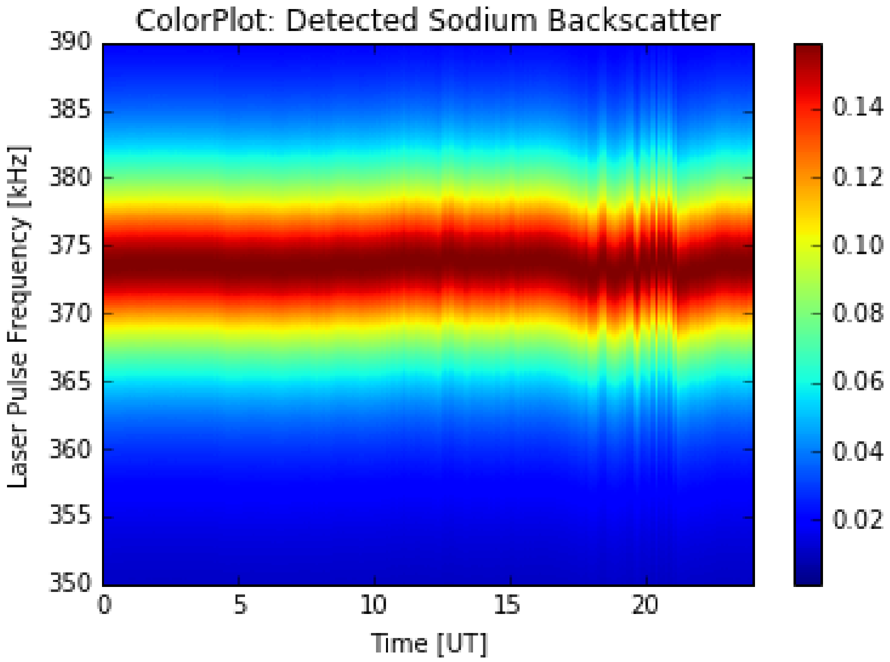

Figure 37: Mockup plot using magnetometer data from January 3, 2017, a day of average magnetic activity. Data from Tromsø Geophysical Observatory[46].

An example of the same model for a magnetically active day is given in Figure 38. This plot was made using the same magnetometer data from Andenes as Figure 35, from the night of October 16, 2016.

Figure 39 shows a zoomed version of the time interval with most disturbance in Figure 38. This shows us that, at least for ground magnetometer data, even rapid magnetic field fluctuations are over timescales on the order of 30 minutes to an hour, and should be resolvable using this method.

Of course, without magnetic data for the mesospheric regions where these measurements are to take place, it is hard to know the realistic speed and intensity of fluctuations. This is a quantity that will be further understood only by actual experimental measurements of this sort. In the event of rapid magnetic field fluctuations, it should be possible to adjust the PRF range accordingly, with only small additions to total sweep time. We will spend some time in the next chapter discussing potential problems and error that may be encountered in realistic measurements.

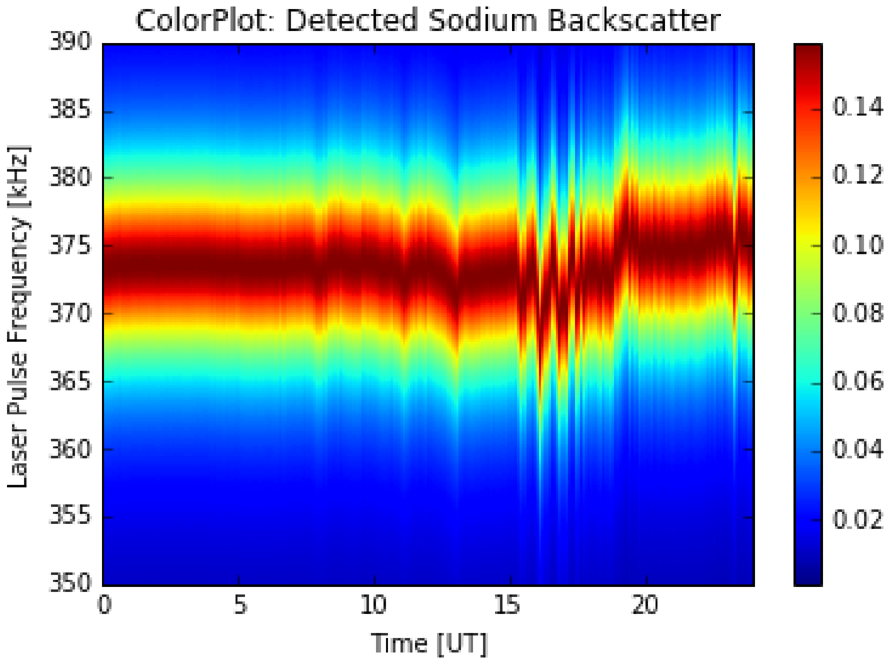

Figure 38: Mockup plot using magnetometer data from October 16, 2016, a relatively active day. Data from [46].

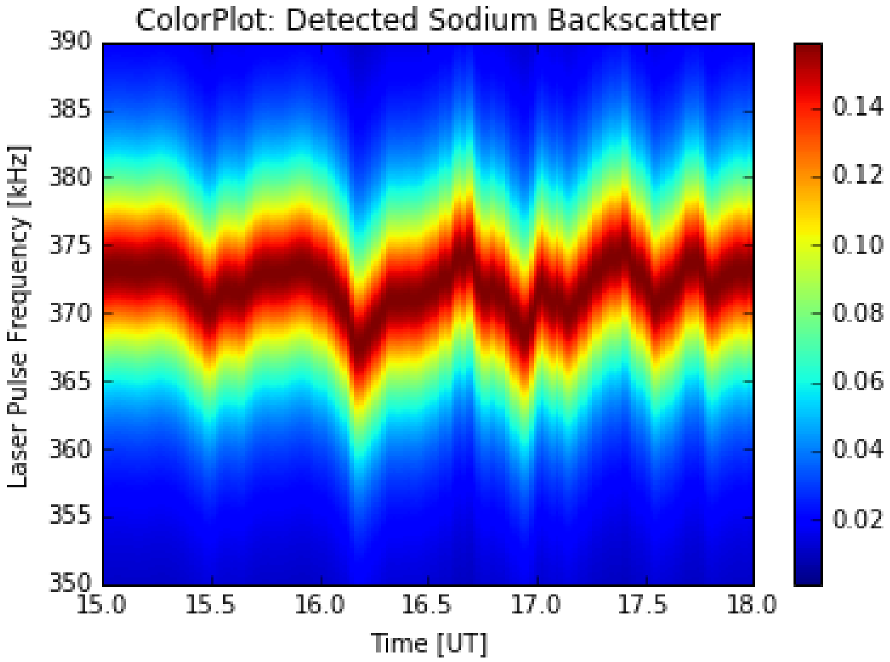

Figure 39: Zoomed plot to show noisy region of Figure 38.

7

DISCUSSION AND CONCLUSION

7.1 DISCUSSION: RESONANCE SIMULATIONS

The simulations presented in the previous chapter confirm the existence of a fluorescence peak at a Larmor-resonant laser pulse frequency. The advantages of using circularly polarized laser light have been demonstrated; the mapping of atomic population in Figure 28 model the orientation of sodium to the preferential (F=2,m=+2) state, and Figure 31 further illustrates the tendency of unoriented atoms to become lost to the laser excitation process. These help to confirm the analysis of atomic processes as covered in Chapter 3.

The shape and positioning of the resonance peak simulations indicates that there are still many things left unexplained, and given time constraints, they are presented with the best current understanding. It is my intention to organize this final chapter in a way that is helpful to any future student continuing with the project, and that by going forward, the existing questions may readily be answered.

The biggest overall obstacle in creating accurate simulations, both for replicating past work and for estimating the results at ALOMAR, is time. Each individual value of Φ calculated for a single point in the resonance plots takes between 1-2 hours to simulate, even after minimizing the number of calculated irradiance levels (the program only allows a minimum of 2) and the number of simulated pulses to achieve a realistic return flux value (7 pulses were deemed sufficient for the flux value to stabilize, after running a few test long-plots).

With the available time for running simulations, the Φ values were made purposefully sparse to achieve an overall sketch of the resonance curves. More thorough simulations using LGSBloch could also help to better understand the actual shape of the resonance curve, which for ease has been modeled here as Gaussian.

The following subsections will discuss our resonance curve simulations and the most pressing questions regarding the results.

7.1.1 *Resonance Signal and FWHM*

In order to obtain an overall "sketch" of the simulated resonance peaks, the points were fit to a Gaussian distribution. It is uncertain whether this is the best choice of fit; Higbie et al. modeled their points using a Lorentzian, while Kane et al. modeled with a triangle function. From our bare data points, it is hard to determine where, or even if, the return flux reaches a "background" level. The shape of our plots resemble something of a mix between those modeled by Higbie et al. and those measured by Kane et al. The width of the peaks, however, are never as well-defined as those in the former, and resemble the latter in this respect.

Table 7 gives a summary of approximate proportional increase of each resonance plot and the FWHM of the curve. The approximate % increase is calculated by dividing the highest peak value by the Gaussian "floor" value and taking the remainder.

Table 7: Simulation Flux Increase & FWHM

Figure Reference	Approx. % Increase	FWHM [kHz]
Figure 29	15%	40
Figure 30	3%	30
Figure 32	0.5%	45
Figure 33	30%	50
Figure 34	16%	70

with the values from Figure 30 and Figure 33 taken as unreliable, since there are no points mapping the "floor" of each Gaussian curve. They are included here simply for completeness.

The biggest contributer to resonance increase is the angle of the laser beam with respect to the magnetic field lines. This is demonstrated quite well with our simulations, following assertions made by Rachel Rampy[53], Fan et al.[19], and James Higbie that the resonance peak will diminish as the laser beam approaches parallel to the magnetic field lines.

It is probable that atmospheric conditions during actual measurements can also have a dampening effect on the height of this resonance peak. A few experimental plot points showed that factors like atmospheric transmission (T_a), sodium column density C_{Na}, and mesospheric spot size have significant effects on the amount of return scatter.

Compared to the model given by Higbie in Figure 2, all of our simulated resonance curves decrease much less sharply. Theoretically, the relative width of these curves are dependent on velocity groups and Doppler broadening from atomic motion, which were not specified in Higbie et al., so it is possible that our spread is indeed more realistic.

This seems to be supported by the experimental measurements done by Kane et al. Figure 3 does exhibit a less well-defined "floor" than Higbie et al., at least within the given frequency range, with a continual decrease in return flux within 20 kHz to either side of the peak.

As mentioned at the beginning of this section, the Gaussian fits should be taken with some skepticism, since the minimal number of plot points computed may be insufficient to produce a realistic model of the resonance curve.

7.1.2 *Resonance Peak Shift*

The most surprising outcome of our LGSBloch simulations was the tendency for resonance peaks to shift away from the Larmor frequency at angles farther from orthogonal.

A summary of the resonance peak values, both calculate and as appearing in the LGSBloch simulations, is given in Table 8, where *Angle* Θ corresponds to the angle between the laser beam and magnetic field lines.

Table 8: Simulation Plot Resonance Peaks

Figure Reference	Angle Θ	Calculated PRF [kHz]	Sim PRF [kHz]
Figure 29	90°	350	350
Figure 30	60°	317	313
Figure 32	168.14°	356.8	335
Figure 33	90°	356.8	357
Figure 34	138.14°	357.1	349

The experimental results of Kane et al. support that this is the result of a problem within the simulation and not an unaccounted physical phenomenon. It is clear from Table 8 that there is an angular dependence on the peak shift, though Kane et al. report measuring with laser beam oriented 60° from the local magnetic field lines, and observed the expected magnetic field value. As the main purpose of remote laser magnetometry is to locate the exact position of this resonance peak, this is perhaps the most important necessary follow-up for further studies on the subject.

Because the Mathematica program does not use an external magnetic field reference, such as IGRF, and only calculates based on user-defined geometry, altitude, and magnetic field strength, it is most likely that the problem lies simply within the input of environmental parameters. It is unfortunately a matter of time constraint in resolving the issue, and it will be necessary for any follow-ups to spend more time going through the Mathematica code to determine if there are any logical errors in input parameters.

7.2 DISCUSSION: LONG-TERM SIMULATIONS

All of the long-term models were used assuming the characteristics (amplitude of resonance peak and FWHM) of our 30°-ALOMAR resonance curve in Figure 34. Magnetic field data was taken from ground-based magnetometers in Andenes.

These color plots give a good example of how we will visualize data from remote laser magnetometry observations. These are presented under the assumption that curve characteristics are indeed realistic for actual flux measurements, and that magnetic field fluctuations at 90km resemble those on the ground, which is likely untrue.

From these simulations, very little can be determined about accuracy in magnetic field measurements using this method. We can, however, discuss some constraints on the system that give a lower limit to measurement accuracy. Error within our measured magnetic field values is mainly introduced by the step size within our frequency sweep. With a step size of 1 kHz, for example, we can use the inverse of Equation 6, to determine that this corresponds to a magnetic field resolution of approximately 150 nT . The Brimrose AOM at ALOMAR cites a step size less than 1Hz, which could theoretically yield magnetic field resolution of ≈ 0.2 nT[1], though this seems extremely ambitious.

The colorplot mockup figures do show that we will need quite a large sweep of frequencies to catch the disturbed regions during magnetically active periods of time. Since our pulse frequencies are in the range of $300-400$ kHz, a full sweep still corresponds to a reasonably short time period. If, for example, we pulse between $350-400$ kHz with 1 Hz step size, the total sweep time remains under one second. It should be reasonable to have good time resolution of measurements every second or few seconds.

Shifts in atomic velocities in the mesosphere will make achieving magnetic field resolution even more challenging, since noise will inevitably be introduced and peak detection will be less well-defined.

It is possible that using a larger-linewidth laser may aid in mitigating this error. Laser linewidth is defined by the spread of actual light frequency around sodium resonance wavelength of 589 nm. Having some of the laser light tuned slightly above and below this resonant wavelength means that a larger percentage of the light can interact with atoms in motion, for whom the light frequency will be Doppler shifted[53].

It is worthwhile attempting more simulations with varying laser linewidth values to see how effective this approach may be.

7.3 FOLLOW-UPS AND DEVELOPMENTS

Other than the need for further modeling, there is the opportunity for exploration within the subject of laser magnetometry. First, I will discuss a proposition from James Higbie regarding the use of linearly polarized light at high latitudes, which includes some discussion of atomic physics. It appears in the conclusion because its relevance goes only insofar as it is an interesting thought for a related experiment. It also deserves to be mentioned in order to avoid confusion at the statement made in [29].

Second, I will discuss some of the criteria that is necessary in order to install a functional laser magnetometry system at ALOMAR that also allows for the concurrent use of sodium lidar.

Finally, I will discuss shortly ideas for observing vector magnetic field values, i. e., the possibility of using remote methods to determine the direction of magnetic field fluctuations.

7.3.1 *The Question of Linear Polarization*

James Higbie proposes offhand at the end of his 2010 paper[29] the possibility of using linearly polarized light to probe hyperfine populations:

> We note also that at the cost of increasing the relaxation rate, the excited-state hyperfine structure can be spectrally resolved by using a narrow-linewidth laser, potentially allowing detection of magneto-optical resonances involving higher polarization multi- poles such as alignment (prepared by pumping with linearly polarized light) (10). This capability has the additional practical implication that magnetic fields in the mesosphere could be effi- ciently sensed in regions (e.g., near the poles) where the Earth's magnetic field is near-vertical. In such locations it is more prac- tical for the pump laser beam to be parallel to the field than perpendicular, a geometry suitable for magnetometers based on atomic alignment but not for those employing atomic orientation[29].

This describes an altogether different experiment from the one outlined in this thesis, one utilizing a narrow-linewidth laser to resolve the D_{2a} and D_{2b} hyperfine transitions and observe resonances associated with them. This instead prepares the atoms using linearly polarized light, which creates atomic *alignment* – distinct from atomic *orientation*, as will be explained further below. This setup, he proposes, can then be used to detect alignment-resonance in polar regions, purely as a theoretical alternative based on the geometry of an observatory at high latitudes.

Section 3.2.2 and Section 3.3.2, in the chapter on atomic physics, cover the concept of atomic *orientation*: using circularly polarized laser light to take advantage of atomic selection rules and force sodium valence electrons into the (F=2,m=+2) state. As discussed in Section 3.2.2, this is equivalent to "pointing" (orienting) the angular momentum axis in the same direction.

Alignment, on the other hand, favors a given axis as opposed to a single direction. This is the equivalent of having two antiparallel *orientations*; for example, inducing sodium valence electrons into either the (F=2,m=+2) state or the (F=2,m=-2) state[48]. A figure illustrating this, and a more pedantic definition of the two terms, can be found in Appendix A.

One can imagine that signal from alignment is less than that of orientation, and it is in fact, "negligible" in comparison[20].

With this knowledge, we can then understand qualitatively the way that linearly polarized light only creates alignment, and so does not possess orientation. The symmetry axis of linearly polarized light is defined as the polarization direction, which points in two directions orthogonal to the propagation direction.

Circularly polarized light, contrarily, induces both alignment and orientation in one preferential direction because the symmetry axis is along the laser propagation direction, and does not include the antiparallel direction[20].

In the context of our experiment, it remains advantageous to maximize laser angle and simply take advantage of the perpendicular component.

7.3.2 *Concurrent Lidar & Magnetometry*

ALOMAR observatory uses lidars primarily for atmospheric research, measuring quantities like particle densities, temperature, and wind speeds. It is worthwhile to comment on how a laser magnetometry project such as this may overlap with lidar research. Is it possible to engage the same laser beam for remote magnetometry while simultaneously making traditional lidar measurements? The major considerations in this regard are laser spot intensity on the mesosphere, and available information given laser pulse frequency. I will cover each individually.

For lidar experiments, light intensity is relatively low at the altitude of the sodium layer. The current Weber sodium lidar at ALOMAR exits the telescope hall with a beam diameter of $20mm$ and full-angle beam divergence of $450\mu rad$[17]. This corresponds to an illuminated area of approximately $1288m^2$ at $90km$. Even for a laser like the Toptica sodium laser at $10W$, this results in an irradiance of $0.008W/m^2$, an extremely low value for magnetometry.

Since so much of laser magnetometry depends on increasing the return backscatter from mesospheric sodium, the use of a beam-expander to narrow laser spot size on the mesosphere is the most straightforward method of increasing light intensity. The only upper limit would appear to be the avoidance of intensities high enough to cause the majority of sodium atoms to undergo stimulated emission rather than spontaneous emission (backscatter).

Rachel Rampy[53] has an explicit breakdown of the laser format efficiencies at numerous irradiance levels, as the question is not simply a matter of maximizing laser intensity. Rampy concludes that an irradiance of $31.4W/m^2$ achieves the highest specific return, which is not especially reasonable given our setup.

However, it should be possible to manage a reasonable mesospheric spot size, changeable between lidar measurements and magnetometry measurements, with the use of a beam-expanding telescope.

There is an issue with our high pulse frequencies for laser magnetometry. To make traditional lidar measurements with a laser, pulse frequency is much smaller, around 50 Hz[17], corresponding to a longer physical length of the laser pulse at the sodium layer. This is used to resolve altitude variations within the sodium layer, which is not possible using such shorter pulses as 350 kHz.

However, there is the possibility of utilizing a "micro/macro" pulse regime, as is the case for LGS systems at the University of Adelaide and Palomar[33]. This creates two overlapping pulse frequencies, potentially arranged to have 350 kHz "micro"pulses with a burst of higher power output, or "macro"pulses, closer to 50 Hz.

7.3.3 *Range-Resolved Magnetometry*

Kane et al. briefly discuss the subject of range-resolved magnetometry, or observing a steeper angle of the laser beam within the sodium layer to achieve greater spatial resolution of magnetic field measurements. This is possible by widening the telescope baseline, and increasing the distance between the transmitter and receiver telescopes, so that the receiving telescope sees the transmitted beam passing through its field of view at an angle[42].

The geometry of this is shown in Figure 40

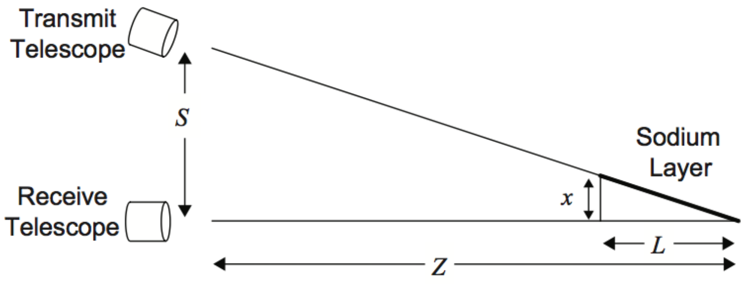

Figure 40: Geometry enabling range-resolved magnetometry, by widening the separation between transmit telescope and receiver telescope. x is the apparent beam size, in meters, of the beam in the sodium layer, as seen by the receiver. Figure from [42].

with x as the apparent beam size in the sodium layer, as seen on the ground, Z is distance to the sodium layer, with thickness L. The separation, S, can be determined by the desired beam spot size. This creates an extended source in the view of the receiver telescope, elongating the visible laser spot size in the mesosphere. The illuminated area can then be broken up and measured at separate distinct spots, with magnetic field measurements corresponding to different altitudes. In this case, return signal from each spot will be a fraction of the total signal, since the beam spot is measured as separate parts[42].

Another method is to use a laser pulse frequency at a subharmonic of the Larmor frequency. This should be possible, since sodium spin-relaxation time is long compared to the Larmor frequency. Altitude could then be determined by time-gating the detector[42].

7.4 CONCLUDING REMARKS

Given even a short few months, I am confident that the programming and modeling issues can be resolved, providing a more ideal representation of observational results. The Mathematica code used for simulations should be investigated to ensure accuracy in our modeling attempts, though I am optimistic that this issue is a minor one.

In moving forward, the most important step is to gain a more thorough understanding of these simulations. It will be necessary to create backscatter spectra like those in Figure 29–Figure 34 with a larger number of data points. This will aid in determining the best fit to the resonance curve, and how distinguishable the peak truly is from the "background" sodium flux, i. e., what determines this background and where it can be defined.

The largest obstacle in modeling these curves was time. Future students may find it worthwhile to run simulations on a more powerful computer than an ordinary desktop. For someone more familiar working in Mathematica, it may merit rewriting the code to calculate a full sweep of frequencies at once rather than one data point at a time, to save more time.

Once accurate and complete curves have been produced, some questions can then be more thoroughly investigated – most importantly, what governs the width of the resonance peak and the resonance signal-to-noise. This then opens the door to other important pursuits, including quantification of constraints on laser beam angle with the magnetic field, and what conditions make it feasible to measure with the laser beam oriented at zenith. Changes in mesospheric and atmospheric conditions and how they would affect backscatter return can also be better understood.

Additionally, it is prudent to undertake further tests and analyses of the hardware components to become entirely familiar with the experimental setup in action. In this case, further error that may be introduced into the system can be more accurately quantified. In addition, some further work solidifying how to combine this project with traditional lidar measurements is also a useful pursuit.

Remote laser magnetometry is a novel method, but one that can be utilized effectively for the detailed observation of magnetic fields in a region that currently has little physical study. Because of the laser infrastructure already in place in northern Norway at ALOMAR, there are only few additional considerations before observation can be initiated. Further refinement of theoretical modeling is necessary to assess expected magnetic field strengths and their variations within the mesosphere with our two possible laser systems.

Once this has been achieved, the most important further work is actual experimental measurements. The advent of remote laser magnetometry is a promising addition to the legacy of magnetic field observation in northern Norway, and its commencement is certain to provide profound insight into Earth's magnetic field.

Part IV

APPENDICES

A

APPENDIX A – CONFUSING TERMINOLOGY

The nexus of atomic, optical, and atmospheric physics in this experiment has led to several unfortunate overlaps in terminology. Throughout this thesis, I have endeavored to be as clear as possible with these terms in order to avoid confusion. I am well aware, however, of the annoyance at encountering similar words with very different meanings, and so have included this appendix in the hope of saving any future students from the confusion I experienced.

A.1 FREQUENCY

The most commonly repeated word in this subject is unquestionably *frequency*. It may refer to any of the following:

- The wavelength, or "color", of the laser light. This is usually referred to simply as the *laser frequency* or *light frequency*, though I have tried, when possible, to use the word *wavelength* for clarity, or to specify *589 nm light*.
- The rate at which the laser beam is pulsed, i. e., the rate at which the laser light is turned from an *off* state to an *on* state. This may be called the *pulse frequency*, *pulse repetition frequency*, or *PRF*.
- The *Larmor frequency*, a naturally occurring rate at which an atomic dipole precesses when subjected to a magnetic field. When referring to this phenomenon, I have tried to always specify *Larmor frequency*. This may cause confusion due to the fact that, in our case, we aim to match the PRF and Larmor Frequency.
- The rate at which a full sweep of laser PRF is conducted. Within the experiment, the laser pulse frequency is varied, starting at a lower value and moving to a higher value, then repeating. The rate at which this full cycle is completed I denote the *sweep frequency*, though thankfully it is discussed briefly in this thesis.

A.2 RESONANCE

Though the term resonance is generally defined as "when two separate frequencies match", the above section hints at how this word, too, can lead to confusion. Resonance is used to denote the following:

- The wavelength of laser light matching a specific energy transition within the sodium atom, so as to cause absorption. This is usually what is meant when the phrase *resonant light* is used.

- Laser pulse frequency matching the sodium Larmor frequency. Here we have two terms contained within one phenomenon: the *resonance* of the laser pulses with the spinning of sodium atoms (i. e., $\mathrm{PRF} = f_L$), which in turn leads to *resonant backscatter* from the sodium. This is discussed in Section 3.3.3.

A.3 POLARIZATION

Polarization is perhaps the term used with most abandon in the surrounding literature. As with the other terminology, I have tried to parse these meanings, in the following manner:

- *Light polarization* or *laser polarization*. This refers specifically to the polarization of the light of the laser beam, i. e., whether linearly or circularly polarized light is being emitted.

- The preferential direction of scattered light from the sodium atoms is often called the *scatter polarization*, or, unhelpfully, also the *light polarization*. When discussing the angular preference of scattered light from sodium, I have tried to simply use *direction*.

- The population of specific atomic states is often referred to as the atom's polarization. This refers to the directionality of the spin axis of the atom, caused by the atomic state. In this case, I have avoided use of the word *polarization* altogether, and instead opt for either *alignment* or *orientation*, which I will define in the following section. The inclusion here is merely to warn the reader of this use within other literature.

A.4 ALIGNMENT VS. ORIENTATION

Alignment and *Orientation* have specific definitions within atomic physics. For the purposes of this thesis, the terminology is used when referring to sodium atomic states, i. e., the directionality of the atomic spin axis (this is equivalent to discussing the population of m atomic states within an atom).

This is covered within the thesis in Section 3.3.2 and further in Section 7.3.1, but for clarity, is also included here. Figure 41 gives a visual representation of the two terms.

- A single atom, or ensemble of atoms, is said to be *oriented* when they preferentially point in one direction. This is equivalent to saying the atoms preferentially populate one maximum m atomic state and have depopulated the rest.

- *Alignment* describes an ensemble of atoms whose spin axes point along a line, either parallel or antiparallel. The term applies when there is no single net direction, but rather a symmetry

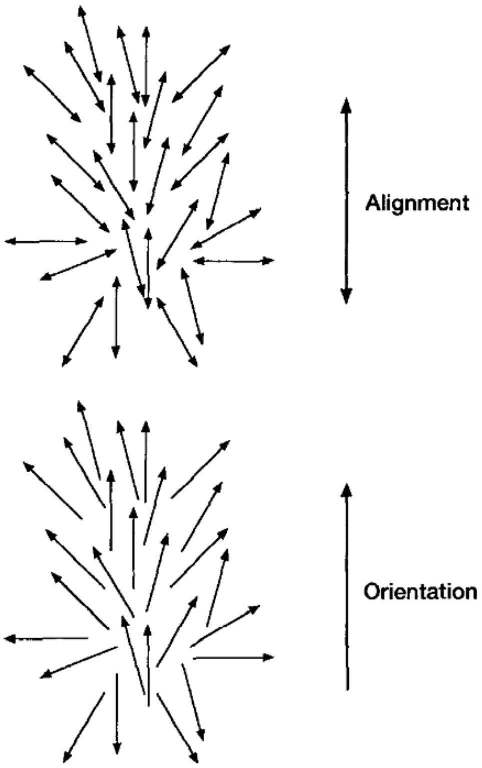

Figure 41: A visual description of alignment and orientation. Image from Andrew J. Orr-Ewing and Richard N. Zare[48].

axis. This is equivalent to saying the atoms preferentially populate both $\pm m$ and depopulate states in between.

A.5 PULSING VS. PUMPING

Though there is not repeated terminology here, the two are similar enough to cause confusion. The distinction is fundamental for this experiment, so I have included it in this appendix.

- *Pulsing* refers to the switching of the laser beam from an *off* state to an *on* state.
- *Pumping* refers to the process of optical pumping, i. e., the use of circularly polarized laser light to induce sodium atoms into a specific atomic state, specifically, raised to an energy level just above the lowest ground state. This is covered in Section 3.3.2.

B

APPENDIX B – MISCELLANEOUS

B.1 CONTENTS OF PARAMS.TXT

The following is an example of the contents of the LGSBloch `params.txt` file, intended to familiarize any future student with how to input parameter values in the `SimPulsedShow` and `SimPulsedLGSParallel` programs. These parameters were used were used for generating information shown in Figure 27–Figure 34. All parameters are input into a text file resembling the following, which is loaded into the programs using the terminal command:

```
nohup nice -n 20 math < driverParallel.m > log.txt &
```

```
(* Testing Larmor resonant chirping with 6 discrete frequencies,
separated by 40 MHz *)

(* FWHM pulse duration [s] *)
tPulse -> 0.2*(1/356845)

(* Number of pulse samples to use (1: square pulse of length
  tPulse). Use odd number. *)
pulseSampleN -> 1

(* Micro pulse rep time [s] *)
trepMicro -> tPulse/0.2

(* Rep time for StepPulseFlux[] [s] *)
trepSim -> trepMicro

(* Macro pulse duty cycle, hence ratio of macro pulse duration
  to rep time (use 1.0 for no macro pulses) *)
dutyMacro -> 1.0

(* Concentrate the light to every brightPeriodSkip'th period
  (use 1 for no skipping) *)
brightPeriodSkip -> 1

(* Angle theta between laser and field lines [deg] *)
magZenithDeg -> 168.14

(* Laser central frequency offset [Hz] as a function of time [s] *)
\[CapitalDelta]fLaserFunction -> (0.0&)
```

```
(∗ Mesospheric effective Gaussian beam FWHM [m] ∗)
FWHMmeso -> 20

(∗ Number of irradiance samples to compute ∗)
iMesoStepN -> 3

(∗ Ratio of max irradiance to iMeso (do not change from
  2.0 unless you know what you’re doing) ∗)
iMesoMaxMult -> 2.0

(∗ Number of micro pulse periods to simulate ∗)
nPeriods -> 7

(∗ Maximum time between adjacent time samples
for {bright,dark} span [s] ∗)
maxSampleTimePeriods -> 16.25∗^-9 {2,2}

(∗ RepumpingFraction: Laser repumping power fraction
  (D2b power divided by D2a+D2b) ∗)
(∗ LightPolarization: Laser polarization state ∗)
(∗ FWHMbw: Short-term laser FWHM bandwidth (spectral
  envelope) [Hz] ∗)
(∗ Parameters of PsiMeso[] ∗)
optPsiMeso -> {PLaunch -> 10.0, Htele -> 380.0,
  Ta -> 0.9, Zenith -> 0.0∗Pi/180.0,
  RepumpFraction -> 0.2, LightPolarization -> 1.0, BG -> 0.5099,
  MagneticZenith -> magZenithDeg∗Pi/180.0, FWHMbw -> 400000}

(∗ Parameters of StepPulseFlux[] ∗)
optStepPulseFlux -> {VerbosityLevel -> 4,
  RefineResult -> {}, VGMethod -> FixVG,
  InitialState ->{LightOff,uniformIntervalVG[{
  -(9/6∗100.0∗^6+20.0∗^6),9/6∗100.0∗^6+70.0∗^6},30.0∗^6,0.05,100]},
  Tolerance -> 10.0^(-7), TerminationThresh -> 1.0∗10^(-4),
  VGfreezePeriod-> 0}

(∗ File name stub of result output files ∗)
fnameres -> "res"

(∗ Mathematica notebook file name,
containing the routine SimPulsedLGS[]∗)
nbFile -> "SimPulsedLGS.nb"
```

B.2 LARMOR FREQUENCY LOOKUP

The following plots can be used as a quick reference for sodium Larmor frequency in a given magnetic field.

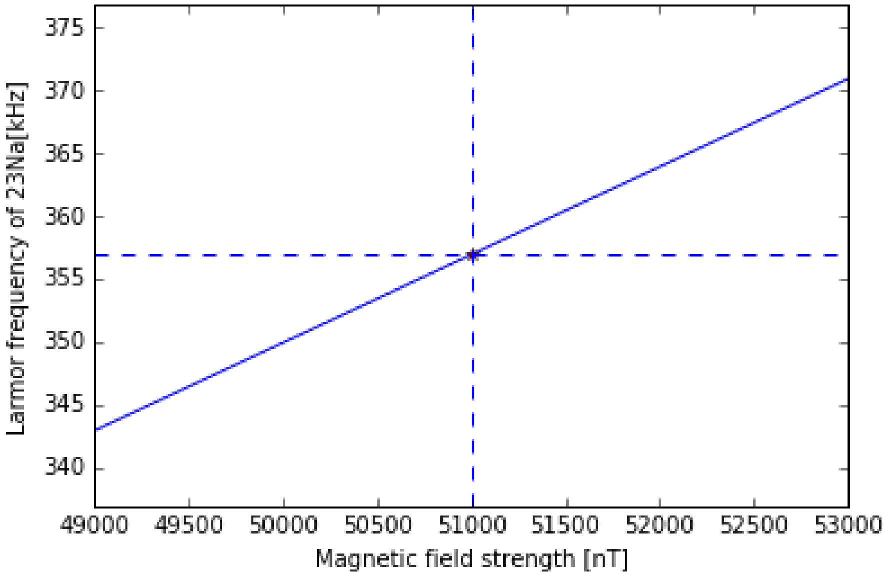

Figure 42: Larmor/pulse frequency range of an average sweep. Approximate magnetic field strength at ALOMAR is marked.

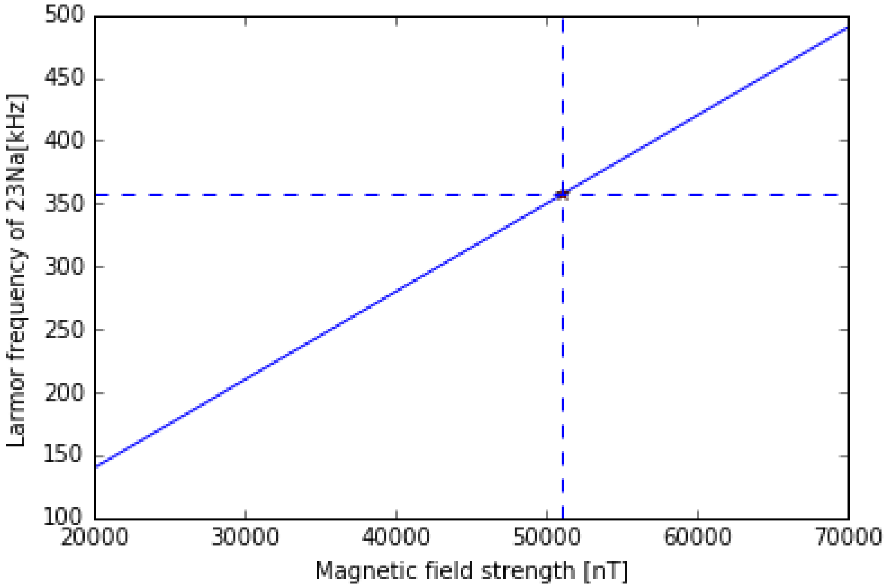

Figure 43: General lookup for total magnetic field range on Earth, as of 2005. Approximate ALOMAR field strength is marked.

B.3 LARMOR FREQUENCY LOOKUP – CODE

For finding a specific value of sodium Larmor frequency/laser pulse frequency, I have included the simple code that can be run in Python, which takes user input magnetic field (in nT) and returns the corresponding Larmor frequency (in kHz) , with an accompanying plot.

```
# -*- coding: utf-8 -*-
"""
Created on Thu Oct  6 09:21:11 2016

@author: aserrano
"""

## Want to create a plot showing larmor frequency of 23Na
## versus magnetic field strength.

## Equation: f_L = (g_F * mu_B * B)/h (B in Tesla)
## I SET EVERYTHING UP TO BE IN kHz and nT.
## Hence the factor in the equation below.


import numpy as np
import matplotlib.pyplot as plt


# Definitions
# f_L  = Larmor frequency for 23Na (species determined by g_F)
# g_F  = Hyperfine Lande g-factor for 23Na ground state
# mu_B = Bohr magneton
# h    = Planck’s constant
# B    = External magnetic field strength [nT]


# Constants
g_F  = 0.5                    # [unitless]
mu_B = 9.27400968e-24         # Bohr magneton [J/T]
    # mu_B = e*h_bar/2*m_e
h    = 6.62607004e-34         # Planck’s constant [m^2*kg/s]

# Want B to be x-axis, a range of values from maybe 3e-5 T to 7e-5
# Define B as a range of values. (this is in nT)
B = np.linspace(30000,70000,num=100)

# Now define equation for Larmor frequency.
# 1e-9 factor to convert T->nT
# 1e3 factor to convert Hz -> kHz
```

```
f_L = (g_F ∗ mu_B ∗ (B∗1e-9))/((1e3)∗h)




#Input magnetic field strength
B_in = eval(input("Please enter desired magnetic field strength [nT]:"))
inf_L = (g_F ∗ mu_B ∗ (B_in∗1e-9))/((1e3)∗h)
#value of f_L for input B field strength

print("The corresponding Larmor frequency for 23Na is %s kHz." %inf_L)



# Plot
ax=plt.figure

plt.plot(B,f_L)
plt.plot(B_in,inf_L, color=’red’, marker=’∗’)
plt.xlabel("Magnetic field strength [nT]")
plt.ylim([inf_L-20,inf_L+20])
plt.xlim([B_in-2000,B_in+2000])
plt.ylabel("Larmor frequency of 23Na[kHz]")
plt.axhline(inf_L,linestyle=’--’)
plt.axvline(B_in,linestyle=’--’)
plt.show()
```

BIBLIOGRAPHY

[1] Brimrose Corporation of America. *Acousto-Optic Modulator Spec Sheet*. URL: http://brimrose.com/products/acousto_optics.html.

[2] M. Auzinsh, D. Budker, and S.M. Rochester. “Light-induced polarization effects in atoms with partially resolved hyperfine structure and applications to absorption, fluorescence, and non-linear magneto-optical rotation.” In: *Physical Review* (2009).

[3] William E. Bell and Arnold L. Bloom. “Optically Driven Spin Precession.” In: *Physical Review Letters* 6.6 (1961), pp. 280–281.

[4] Joshua C. Bienfang, Craig A. Denman, Brent W. Grime, Paul D. Hillman, Gerald T. Moore, and John M. Telle. “20 W of continuous-wave sodium D2 resonance radiation from sum-frequency generation with injection-locked lasers.” In: *Optics Letters* 28.22 (2003), pp. 2219–2221.

[5] Kristian Birkeland. *The Norwegian Aurora Polaris Expedition (available online via archive.org)*. URL: https://archive.org/stream/norwegianaurorap01chririch#page/n5/mode/2up.

[6] Felix Bloch. “Nuclear Induction.” In: *Physical Review* (1946).

[7] B.H. Bransden and C.J. Joachain. *Physics of Atoms and Molecules*. Longman Scientific and Technical, 1983.

[8] Asgeir Brekke. *Physics of the Upper Polar Atmosphere*. Springer Publishing, 2012.

[9] Encyclopedia Britannica. *Foundations of Atomic Spectra*. URL: https://global.britannica.com/.

[10] Thomas R. Carver. “Optical Pumping.” In: *Science* 141.3581 (1963).

[11] Andøya Space Center. *ALOMAR Observatory*. URL: http://andoyaspace.no/?page_id=19.

[12] Stanford University Solar Center. *The Earth’s Ionosphere*. URL: http://solar-center.stanford.edu/SID/activities/ionosphere.html.

[13] H. Chen, C.Y. She, P. Searcy, and E. Korevaar. “Sodium-vapor dispersive Faraday filter,” in: *Optics Letters* (1993).

[14] Alan Corney. *Atomic and Laser Spectroscopy*. Oxford University Press, 1977.

[15] Berkeley Nucleonics Corporation. *Model 645 Function Generator Spec Sheet*. URL: http://www.berkeleynucleonics.com/model-645.

[16] S.W.H. Cowley. “Magnetosphere-Ionosphere Interactions: A Tutorial Review.” In: *American Geophysical Union* (2000).

[17] Tim Dunker. *Effects of meteors and dynamics on the mesospheric sodium layer over Andøya measured with the ALOMAR Na lidar*. 2011.

[18] Tim Dunker. “Lidar measurements of mesopause region temperature and Na number density.” PhD thesis. UiT, The Arctic University of Norway, 2015.

[19] Tingwei Fan, Tianhua Zhou, and Yan Feng. “Improving sodium laser guide star brightness by polarization switching.” In: *Nature Scientific Reports* (2016).

[20] I. Fescenko and A. Weis. “Imaging magnetic scalar potentials by laser-induced fluorescence from bright and dark atoms.” In: *Journal of Physics D: Applied Physics* 47 (2014).

[21] Richard Feynman. *The Feynman Lectures on Physics, Vol. II (available online via Caltech)*. URL: `http://www.feynmanlectures.caltech.edu/II_34.html`.

[22] How Things Fly. *Layers of Earth’s Atmosphere*. URL: `http://howthingsfly.si.edu/media/layers-earths-atmosphere`.

[23] R. Foy and A. Labeyrie. “Feasibility of adaptive telescope with laser probe.” In: *Astronomy and Astrophysics* (1985).

[24] Galileo Spacecraft Fundamental Technologies. *Anatomy of a Magnetosphere*. URL: `http://galileo.ftecs.com/stone-diss/1-anatomymag.html`.

[25] Hermann Haken and Hans Cristoph Wolf. *The Physics of Atoms and Quanta*. Springer Publishing, 2005.

[26] Edmund Halley. *An account of the cause of the change of the variation of the magnetic needle; with an hypothesis of the structure of the internal parts of the earth*. Philosophical Transactions of Royal Society of London, 1692.

[27] W. Happer, G.J. MacDonald, C.E. Max, and F.J Dyson. “Atmospheric-turbulence compensation by resonant optical backscattering from the sodium layer in the upper atmosphere.” In: *Optical Society of America* 11.1 (1994), pp. 263–276.

[28] William Bruce Hawkins. “Orientation and Alignment of Sodium Atoms by Means of Polarized Resonance Radiation.” In: *Physical Review* 98.2 (1955).

[29] James M. Higbie, Simon M. Rochester, Brian Patton, Ronald Holzlöhner, Domenico Bonaccini Calia, and Dmitry Budker. “Magnetometry with mesospheric sodium.” In: *PNAS* 108.9 (2011), pp. 3522–3525.

[30] James Higbie, Ron Holzlöhner, Simon Rochester, Brian Patton, Domenico Bonaccini Calia, and Dmitry Budker. “Using lasers to measure magnetic fields.” In: *SPIE Newsroom* (2011).

[31] J. Hildebrand, G. Baumgarten, J. Fielder, Ulf-Peter Hoppe, B. Kaifler, F.-J. Lübken, and B.P. Williams. “Combined wind measurements by two different lidar instruments in the Arctic middle atmosphere.” In: *Atmospheric Measurement Techniques* 5 (2012), pp. 2433–2445.

[32] Paul D. Hillman, Jack D. Drummond, Craig A. Denman, and Robert Q. Fugate. “Simple model, including recoil, for the brightness of sodium guide stars created from CW single frequency fasors and comparison to measurements.” In: *SPIE Proceedings* (2008).

[33] Ron Holzlöhner, Simon M. Rochester, Domenico Bonaccini Calia, Dmitry Budker, Thomas Pfrommer, and James M. Higbie. “Simulations of Pulsed Sodium Laser Guide Stars – An Overview.” In: 8447 (2012).

[34] Ronald Holzlöhner, S.M. Rochester, Domenico Bonaccini Calia, and Dmitry Budker. “Optimization of cw sodium laser guide star efficiency.” In: *Bucknell Digital Commons* (2010).

[35] Ulf-Peter Hoppe. *Active Remote Sensing from Satellite Platforms by LIDAR*. Norwegian Defense Research Establishment, 1997.

[36] Ulf-Peter Hoppe and Magnar Gullikstad Johnsen. “The mesospheric sodium layer as a remotely, optically pumped magnetometer for investigation of Birkeland currents - Mesospheric Optical Magnetometry (MOM).” 2016.

[37] Leibniz-Institut für Atmosphären Physik IAP. *The ALOMAR RMR lidar*. URL: `https://www.iap-kborn.de`.

[38] Istituto Nazionale di Geofisica e Vulcanologia INGV. *Elements of the Geomagnetic Field*. URL: `http://roma2.rm.ingv.it`.

[39] T.H. Jeys and et al. “Observation of optical pumping of mesospheric sodium.” In: *Optics Letters* 17.16 (1992), pp. 1143–1145.

[40] Thomas H. Jeys. “Development of a Mesospheric Sodium Laser Beacon for Atmospheric Adaptive Optics.” In: *The Lincoln Laboratory Journal* 4.2 (1991), pp. 133–150.

[41] Magnar Gullikstad Johnsen, Jürgen Matzka, Ulf-Peter Hoppe, and Alessandra Serrano. *The mesospheric sodium layer as a remotely, optically pumped magnetometer for investigation of Birkeland currents - Mesospheric Optical Magnetometry (MOM)*. 2016.

[42] Thomas J. Kane, Paul D. Hillman, Craig A. Denman, Michael Hart, R. Phillip Scott, Michael E. Purucker, and Stephen J. Potashnik. “Laser remote magnetometry using mesospheric sodium.” In: (2016).

[43] Mioara Mandea and Monika Korte, eds. *Geomagnetic Observations and Models*. Springer Publishing, 2011.

[44] *Monolithic Mirror Telescope and the Large Binocular Telescope FASOR Upgrade Kit Final Report and Manual*. FASORtronics LLC. PO Box 50370 Albuquerque, NM 87181, 2011.

[45] N. Moussaoui, R. Holzlöhner, W. Hackenberg, and D. Bonaccini Calia. "Dependence of sodium laser guide star photon return on the geomagnetic field." In: *Astronomy and Astrophysics* (2009), pp. 793–799.

[46] Tromsø Geophysical Observatory. *Geomagnetic Data*. URL: `http://flux.phys.uit.no/ascii/`.

[47] National Oceanic and Atmospheric Administration. *Geomagnetic Calculator, http://ngdc.noaa.gov/geomag-web/*. URL: `http://ngdc.noaa.gov/geomag-web/`.

[48] Andrew J. Orr-Ewing and Richard N. Zare. "Orientation and Alignment of Reaction Products." In: *Annual Review of Physics and Chemistry* (1994).

[49] PhysLink. *What Is the Zeeman Effect?* URL: `http://www.physlink.com/education/askexperts/ae646.cfm`.

[50] Earth Observations (EO) Portal. *Swarm (Geomagnetic LEO Constellation)*. URL: `https://directory.eoportal.org/web/eoportal/satellite-missions/s/swarm`.

[51] Brent Ellerbroek, Enrico Marchetti, and Jean-Pierre Véran, eds. *Investigations of long pulse sodium laser guide stars*. Vol. 8447. SPIE Proceedings, 2012.

[52] Rachel Rampy. "Advancing Adaptive Optics Technology: Laboratory Turbulence Simulation and Optimization of Laser Guide Stars." PhD thesis. UC Santa Cruz, 2013.

[53] Rachel Rampy, Donald Gavel, Simon M. Rochester, and Ronald Holzlöhner. "Toward optimization of pulsed sodium laser guide stars." In: *Journal of the Optical Society of America B* 32.12 (2015), pp. 2425–2434.

[54] Simon M. Rochester. *http://rochesterscientific.com/ADM/*. URL: `http://rochesterscientific.com/ADM/`.

[55] Simon M. Rochester, Angel Otarola, Corinne Boyer, Dmitry Budker, Brent Ellerbroek, Ronald Holzlöhner, and Lianqi Wang. "Modeling of pulsed-laser guide stars for the Thirty Meter Telescope project." In: *Optical Society of America* 29.8 (2012), pp. 2176–2188.

[56] Token Rock. *The Earth's Magnetic Field*. URL: `http://www.tokenrock.com/stock/magneticfield.jpg`.

[57] Daniel A. Steck. *Sodium D Line Data*. 2000.

[58] TOPTICA. *TA-SHG pro Spec Sheet*. URL: http://www.toptica.com/products/tunable-diode-lasers/frequency-converted-lasers/ta-shg-pro/.

[59] Laird A. Thompson and Chester S. Gardner. “Experiments on laser guide stars at Mauna Kea Observatory for adaptive imagery in astronomy.” In: *Letters to Nature* (1987).

[60] ThorLabs. *Shearing Interferometers*. URL: https://www.thorlabs.com/newgrouppage9.cfm?objectgroup_id=2970.

[61] T. Vondrak, J.M.C. Plane, S. Broadley, and D. Janches. “A chemical model of meteoric ablation.” In: *Atmospheric Chemistry and Physics* (2008).

[62] Jørgen Østerpart. *Na lidar measurements during the ECOMA/Geminids campaign with focus on Na peak density and temperature*. 2011.

COLOPHON

This document was typeset using the typographical look-and-feel `classicthesis` developed by André Miede. The style was inspired by Robert Bringhurst's seminal book on typography "*The Elements of Typographic Style*". `classicthesis` is available for both LaTeX and LyX:

`https://bitbucket.org/amiede/classicthesis/`

Final Version as of May 15, 2017 (`classicthesis` version 2.0).